ESO-based robust and high-precision tracking control for aerial manipulation

This article has been accepted for publication in IEEE Transactions on Automation Science and Engineering. This is the author's version which has not been fully edited and content may change prior to final publication. Citation information: DOI 10.1109/TASE.2023.3260874

ESO-Based Robust and High-Precision Tracking Control for Aerial Manipulation

Huazi Cao, Yongqi Li, Cunjia Liu, Shiyu Zhao

***Abstract*—This paper studies the tracking control problem of an aerial manipulator that consists of a quadcopter flying base and a Delta robotic arm. We propose a novel control approach that consists of extended state observers (ESOs) for dynamic coupling estimation, ESO-based flight controllers, and a cooperative trajectory planner. Compared to the state-of-the-art approaches, the proposed one has some attractive features. First, it requires much less measurement information as opposed to the full-body control approaches and hence can be implemented conveniently and efficiently in practice. Second, while the existing approaches estimate the coupling effect based on precise models, the proposed ESOs can do that based on much less information about the system model. The proposed approach is verified by four experiments on a real aerial manipulation platform. The experimental results show that the average tracking error can reach 1 cm by the proposed approach as opposed to 10 cm by the PX4 baseline controller. Although force control is not considered specifically in the approach, the system can complete aerial weaving tasks thanks to the ESOs in the presence of drag forces applied to the end-effector during manipulation.**

***Note to Practitioners*—Aerial manipulators have received increasing research attention in recent years due to their wide range of applications. In this paper, we particularly focus on the high-precision and robust control of aerial manipulators. We propose a novel control approach that consists of extended state observers (ESOs) for dynamic coupling estimation, ESO-based flight controllers, and a cooperative trajectory planner. Four experiments on a real aerial manipulation platform demonstrate the effectiveness of the approach. In future research, we will address the control problem when the aerial manipulator contacts the environment.**

***Index Terms*—Aerial manipulator, Delta arm, Extended state observer, Aerial weaving**

I. Introduction

Aerial manipulators have received increasing research attention in recent years due to their wide range of applications. An aerial manipulator combines a flying base, which is usually a multirotor aerial vehicle, with one or multiple robotic arms. Compared to conventional flying robots such as multirotors, an aerial manipulator can interact with the environment to complete various tasks such as pick-and-place [1], tree cavity inspection [2], contact-based inspection [3], opening/closing of a valve [4], assembly of structures [5]. Compared to ground mobile manipulators, an aerial manipulator can fly to areas that are difficult to reach by humans or ground robots, hence greatly enlarging the scope of manipulation tasks.

Fig. 1: Aerial weaving by an aerial manipulator. The experimental video is available at https://youtu.be/QMjGtBCUi-E.

Aerial manipulation has been studied from various aspects such as platform, control, perception, teleoperation, and co-operation up to now. See [6] and [7] for recent surveys. In this paper, we particularly focus on the high-precision and robust control of aerial manipulators. Different from the control of a multirotor, control of an aerial manipulator is much more challenging due to the multi-DoF robotic arm attached to the multirotor base. The dynamics of the multirotor and the robotic arm are coupled: the movement of the robotic arm and the multirotor base mutually affect each other.

The existing control approaches of aerial manipulators can be divided into two categories: full-body control and separate control. Full-body control requires establishing the nonlinear model of the entire aerial manipulation system and then applies appropriate controller design methods [8]. This kind of approach is promising in terms of control accuracy and robustness if the nonlinear dynamics can be precisely modelled. However, they are challenging to implement in practice because on the one hand the precise nonlinear model is difficult to obtain and on the other hand various measurements required by this approach are difficult to obtain. For instance, the full-body control approach proposed in [9] requires velocities and accelerations of the joints of the robotic arm, which is usually difficult to measure for normal actuators. As a comparison, separate control is easier

H. Cao, Y. Li, and S. Zhao are with the School of Engineering at Westlake University and the Institute of Advanced Technology at Westlake Institute for Advanced Study, Hangzhou, China. {caohuazi,liyongqi,zhaoshiyu}@westlake.edu.cn

C. Liu is with the Department of Aeronautical and Automotive Engineering at Loughborough University, Loughborough, UK. c.liu5@lboro.ac.uk

This article has been accepted for publication in IEEE Transactions on Automation Science and Engineering. This is the author's version which has not been fully edited and content may change prior to final publication. Citation information: DOI 10.1109/TASE.2023.3260874

to implement in practice because it does not require knowing the nonlinear model of the entire system and it merely has a minimal requirement on the measurements. The basic idea of separate control is to control the multirotor base and the robotic arm separately. A literature review on related works is given below.

Up to now, researchers have proposed a variety of separate controllers for aerial manipulators. In the early works, the dynamic coupling between the quadcopter and the robotic arm is ignored to simplify controller design [10]. As a consequence, the control accuracy is relatively low. The work in [11] addressed the dynamic coupling from a mechanical point of view: a sliding battery box was used to compensate for the motion of the robotic arm. However, the performance of this method is limited by the sliding velocity of the battery box. In order to well resolve the problem of dynamic coupling, we need to consider three aspects.

The first aspect is the estimation of the dynamic coupling effects. The work in [12] introduced a variable parameter integral backstepping method to design the quadcopter controller. It can only estimate the coupling torques generated by the displacement of the center of mass from the quadrotor geometry center, which may gain more errors when the velocity of the manipulator increases. The works in [13] and [14] adopted model-based disturbance estimators to estimate the disturbance caused by the manipulators. However, the model-based disturbance estimators rely on accurate models of aerial manipulators that are usually hard to obtain.

The second aspect is the compensation of the dynamic coupling term in the control. To take the external disturbance into account, nonlinear control methods such as sliding mode control [15] and backstepping control [16] are introduced into the motion control of the quadcopter. These approaches treat the dynamic coupling term as unknown external disturbances without estimating it. To suppress the influence of the dynamic coupling term, the works in [12]–[14] integrated mode-based disturbance estimators into controllers to compensate for the dynamics coupling term, requiring the accurate models of the aerial manipulators.

The third aspect is cooperative planning of the trajectories for the multirotor base and the robotic arm. Common approaches for cooperative planning include the closed-loop inverse kinematics (CLIK) method [17], [18], the null space-based method [19], and multiple task-priority inverse kinematics method [20]. However, these methods did not consider the physical constraints and, therefore, the solutions of these methods may be infeasible. Recently, the work in [21] proposed a nonlinear model predictive control (NMPC) method and formulated the cooperative planning problem as a constrained optimization problem. The NMPC method is, however, computationally expensive, which may request high computational power or a low update rate.

The above analysis reveals the limitations in the three aspects of the existing control approaches for aerial manipulation. This paper aims to overcome these limitations by proposing a new framework that incorporates a coupling term estimator, a motion controller, and a cooperative trajectory planner. The proposed algorithms are verified by carefully designed experiments on an aerial manipulation platform. The novelty of the proposed algorithms is summarized below.

1) We propose a partially coupled motion controller. The control of the quadcopter and the delta arm are separate, but based on extended state observers (ESOs) to estimate and compensate for the dynamic coupling between the quadcopter and the manipulator. The controller can be divided into two parts: the flight controller and the manipulator controller. The flight controller is designed by an ESO-based nonlinear control method while the manipulator is controlled by the PID method. The dynamic coupling effect in the mathematical model is divided into two known terms and unknown terms. The known terms are directly used in the flight controller design. The unknown terms are estimated by the ESOs in real time. Compared to [13], [14], the advantage of the proposed ESOs is that they rely on less measurement information for estimating the dynamic coupling. Besides, the closed-loop system with the proposed flight controller converges to predesigned dynamics, which are constituted by four desired subloops that can be continently used to tune control gains. All parameters of the controller can be easily determined with the predesigned dynamics according to the performance requirement.

2) A novel cooperative planner with two modes is proposed to coordinate the motions of the quadcopter and the manipulator. The physical constraints of the aerial manipulator are transformed to reduce the computation cost of the planner. To adapt to different manipulation tasks, two control modes, P-P and E-P, are proposed. The P-P mode, designed based on the CLIK method, can be used when the end-effector and quadcopter track separate trajectories. The E-P mode can be used when the end-effector is required to track a given trajectory while the quadcopter base is not. The E-P mode formulates the planning problem as a quadratic programming (QP) problem. The two modes are applicable to different scenarios. The P-P mode is applicable to pick and place task [22], peg-in-hole task, aerial repair task [23], etc. The E-P mode is applicable to the trajectory tracking task, the pulling/pushing task, etc.

The proposed algorithms are verified by four experiments on an aerial manipulator platform. Unlike the traditional Delta arm, the Delta arm used in this paper drives the joint angles by three four-bar linkages to magnify the control forces [24]. Experiments (including disturbance rejection, end-effector stabilization, and end-effector trajectory tracking) are conducted to validate the novelties. At last, we apply the proposed method and aerial manipulator to the aerial weaving (see Fig. 1), which shows the ability to complete tasks.

The remainder of this paper is structured as follows. Problem setup and preliminaries used in this paper are given in Section II. The control system overview is presented in Section III. Section IV proposes the position control system of the quadcopter base. The attitude control of the quadcopter base is proposed in Section V. Section VI gives the proposed cooperative planner. Then, the experimental verification for

This article has been accepted for publication in IEEE Transactions on Automation Science and Engineering. This is the author's version which has not been fully edited and content may change prior to final publication. Citation information: DOI 10.1109/TASE.2023.3260874

TABLE I: List of important notations.

Σ_I	inertial frame such that the z-axis is in the direction of the gravity vector
Σ_B	body-fixed frame that is rigidly attached to the quadcopter base at its center of gravity.
Σ_D	Delta arm frame that is rigidly attached to the arm base at its center $\boldsymbol{p}_F$.
$\boldsymbol{p}, \boldsymbol{p}_d$	position and desired position of the quadcopter ($\boldsymbol{p} \in \mathbb{R}^3$ and $\boldsymbol{p}_d \in \mathbb{R}^3$) in Σ_I
$\boldsymbol{q}, \boldsymbol{q}_d$	joint vector and desired joint vector of the Delta arm ($\boldsymbol{q} \in \mathbb{R}^3$ and $\boldsymbol{q}_d \in \mathbb{R}^3$)
$\boldsymbol{p}_E, \boldsymbol{p}_{E,d}$	position and desired position of the end-effector ($\boldsymbol{p}_E \in \mathbb{R}^3$ and $\boldsymbol{p}_{E,d} \in \mathbb{R}^3$) in Σ_I
$\boldsymbol{p}_E^D, \boldsymbol{p}_{E,d}^D$	position and desired position of the end-effector ($\boldsymbol{p}_E^D \in \mathbb{R}^3$ and $\boldsymbol{p}_{E,d}^D \in \mathbb{R}^3$) in Σ_D
$\boldsymbol{p}_E^B$	position of the end-effector ($\boldsymbol{p}_E^B \in \mathbb{R}^3$) in Σ_B
$\boldsymbol{R}$	rotation matrix ($\boldsymbol{R} \in SO(3)$) from Σ_B to Σ_I
$\boldsymbol{R}_D^B$	rotation matrix ($\boldsymbol{R}_D^B \in SO(3)$) from Σ_D to Σ_B
ψ, ψ_d	yaw angle and desired yaw angle of the quadcopter ($\psi \in \mathbb{R}$ and $\psi_d \in \mathbb{R}$)
$f, \boldsymbol{\tau}$	total force ($f \in \mathbb{R}$) and torque vector ($\boldsymbol{\tau} \in \mathbb{R}^3$) of the rotors
$\boldsymbol{f}_c, \boldsymbol{\tau}_c$	dynamic coupling force vector ($\boldsymbol{f}_c \in \mathbb{R}^3$) and torque vector ($\boldsymbol{\tau}_c \in \mathbb{R}^3$) caused by the Delta arm
$\boldsymbol{\tau}_M$	torque vector of the Delta arm's actuated joints ($\boldsymbol{\tau}_M \in \mathbb{R}^3$)
$\boldsymbol{p}_F^B$	center position of the Delta arm's base ($\boldsymbol{p}_F^B \in \mathbb{R}^3$) in Σ_B

the proposed methods is given in Section VII. Conclusions are drawn in Section VIII.

II. Problem Setup and Preliminaries

This section presents the problem setup and some necessary preliminary results.

A. Problem setup

The aerial manipulator considered in this paper consists of a quadcopter base and a Delta arm (see Fig. 2). The base of the Delta arm is attached underneath the quadcopter. The position of the end-effector of the Delta arm can be controlled by changing the torques applied to the three actuators fixed on the base. However, the orientation of the end-effector remains the same as the base of the Delta arm [25]. Hence, the Delta arm has three translational DoFs and three control inputs (i.e., the torques applied to the three actuators). On the other hand, the quadcopter base has six DoFs and four inputs (i.e., the thrusts of the four blades). Therefore, the entire system has nine DoFs and seven control inputs.

The aerial manipulator has three reference frames: the inertial frame Σ_I, the quadcopter body-fixed frame Σ_B, and the Delta arm frame Σ_D (see Fig. 2). Σ_I is an inertial frame where the z-axis is in the direction of the gravity vector. Σ_B is rigidly attached to the quadcopter base. Its origin coincides with the center of gravity of the quadcopter. Σ_D is rigidly attached to the Delta arm base at its geometric center $\boldsymbol{p}_F$.

Denote the position of the end-effector in Σ_I as $\boldsymbol{p}_E$. The desired end-effector position in Σ_I is $\boldsymbol{p}_{E,d} \in \mathbb{R}^3$. Let $f \in \mathbb{R}$ and $\boldsymbol{\tau} \in \mathbb{R}^3$ denote the total force and torque vector generated by the four rotors. Let $\boldsymbol{\tau}_M \in \mathbb{R}^3$ represent the torque vector of the Delta arm's actuators. The control objective is to design the control input $f, \boldsymbol{\tau}, \boldsymbol{\tau}_M$ so that $\boldsymbol{p}_E$ can track $\boldsymbol{p}_{E,d}$ accurately.

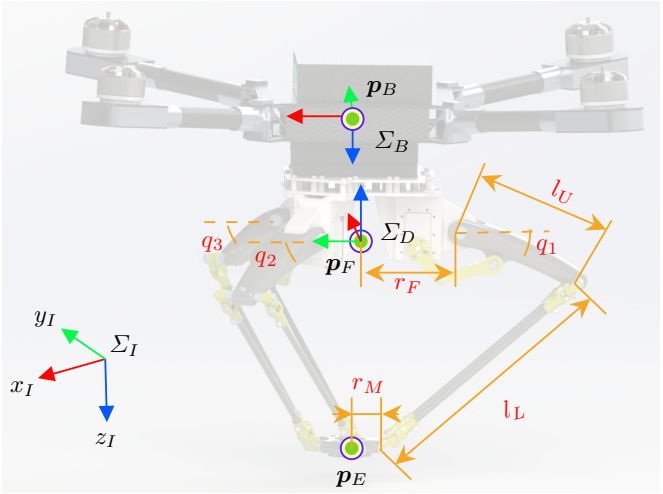

Fig. 2: An illustration of the aerial manipulator.

B. Kinematics of the Delta arm

This subsection describes the kinematics of the Delta arm. Let $\boldsymbol{p}_F^B \in \mathbb{R}^3$ denote the position of the center of the base in Σ_B. Let $\boldsymbol{p}_E^B$ and $\boldsymbol{p}_E^D$ denote the positions of the end-effector in Σ_B and Σ_D, respectively. The relationship between $\boldsymbol{p}_E^B$ and $\boldsymbol{p}_E^D$ is

$$\boldsymbol{p}_E^B = \boldsymbol{R}_D^B \boldsymbol{p}_E^D + \boldsymbol{p}_F^B, \tag{1}$$

where $\boldsymbol{R}_D^B \in SO(3)$ is the rotation matrix from Σ_D to Σ_B.

The lengths for the upper and lower arms are represented by $l_U \in \mathbb{R}$ and $l_L \in \mathbb{R}$ as illustrated in Fig. 2. Circumradii of the top base and the bottom end-effector base are, respectively, defined as $r_F \in \mathbb{R}$ and $r_M \in \mathbb{R}$. The relationship between the end-effector position $\boldsymbol{p}_E^D \in \mathbb{R}^3$ and the joint vector $\boldsymbol{q} = [q_1, q_2, q_3]^T \in \mathbb{R}^3$ is

$$\left\| \boldsymbol{p}_E^D - \boldsymbol{h}_i \right\|^2 = l_L^2, \quad i = 1, 2, 3, \tag{2}$$

where

$$\boldsymbol{h}_i = \begin{bmatrix} -(r_F - r_M + l_U \cos q_i) \cos[(i-1)\pi/3] \\ (r_F - r_M + l_U \cos q_i) \sin[(i-1)\pi/3] \\ l_U \sin q_i \end{bmatrix}. \tag{3}$$

On the one hand, given a joint vector $\boldsymbol{q}$, the position $\boldsymbol{p}_E^D$ can be solved from (2) based on the forward kinematics. On the other hand, given a position $\boldsymbol{p}_E^D$, the joint vector $\boldsymbol{q}$ can be solved from (2) by the inverse kinematics. Details can be found in [26], [27].

As can be seen from Fig. 2, the joint angles of the Delta arm are driven by planar four-bar linkages. The relationship between the joint angles and the crank position angles can be calculated by the kinematics of the planar four-bar linkage [28, Section 3.6].

C. Kinematics of the aerial manipulator

The position of the end-effector in Σ_I can be calculated by $\boldsymbol{p}_E = \boldsymbol{p} + \boldsymbol{R}\boldsymbol{p}_E^B$, where $\boldsymbol{R} \in SO(3)$ is the rotation matrix from Σ_B to Σ_I. The time derivative of $\boldsymbol{p}_E$ is

$$\begin{aligned}\dot{\boldsymbol{p}}_E =& \dot{\boldsymbol{p}} + \dot{\boldsymbol{R}}\boldsymbol{p}_E^B + \boldsymbol{R}\dot{\boldsymbol{p}}_E^B,\\ =& \dot{\boldsymbol{p}} + \boldsymbol{R}\boldsymbol{R}_D^B\dot{\boldsymbol{p}}_E^D - [\boldsymbol{R}\boldsymbol{p}_E^B]_\times\boldsymbol{\omega},\end{aligned} \tag{4}$$

where $\boldsymbol{\omega} \in \mathbb{R}^3$ is the angular velocity vector of the quadcopter expressed in Σ_B, $[\cdot]_\times$ denotes the skew-symmetric matrix. Let

$$\boldsymbol{s} = \begin{bmatrix} \boldsymbol{p} \\ \boldsymbol{p}_E^D \end{bmatrix} \in \mathbb{R}^6.$$

Then, (4) can be rewritten as

$$\dot{\boldsymbol{p}}_E = \boldsymbol{J}\dot{\boldsymbol{s}} - [\boldsymbol{R}\boldsymbol{p}_E^B]_\times\boldsymbol{\omega}, \tag{5}$$

where $\boldsymbol{J} = [\boldsymbol{I}_3, \boldsymbol{R}\boldsymbol{R}_D^B]$ is the Jacobian matrix, $\boldsymbol{I}_3$ is the 3×3 identity matrix.

D. Dynamics of the aerial manipulator

The dynamics of the aerial manipulator can be divided into the dynamics of the quadcopter base and the Delta arm. Inspired by [13], the dynamics of the quadcopter base are surveyed to design the flight controller of the aerial manipulator. The dynamics of the quadcopter base in the aerial manipulator are

$$\begin{aligned}\dot{\boldsymbol{p}} &= \boldsymbol{v},\\ \dot{\boldsymbol{v}} &= \boldsymbol{g} - \frac{\boldsymbol{f} - \boldsymbol{f}_c}{m_B + m_M},\\ \dot{\boldsymbol{R}} &= \boldsymbol{R}[\boldsymbol{\omega}]_\times,\\ \dot{\boldsymbol{\omega}} &= \boldsymbol{M}^{-1}\left[\boldsymbol{\tau} - \boldsymbol{\omega}\times(\boldsymbol{M}\boldsymbol{\omega}) + \boldsymbol{\tau}_c\right],\end{aligned} \tag{6}$$

where $\boldsymbol{v} \in \mathbb{R}^3$ represents the velocity vector of the quadcopter base, $\boldsymbol{g} \in \mathbb{R}^3$ is the gravity vector, m_B represents the mass of the quadcopter base, m_M is the mass of the Delta arm, $\boldsymbol{M} \in \mathbb{R}^{3\times 3}$ denotes the inertia matrix of the quadcopter base, $\boldsymbol{\tau} \in \mathbb{R}^3$ represents torque vector of the rotors. In addition, $\boldsymbol{f} = \boldsymbol{R}[0,0,f]^T \in \mathbb{R}^3$ is control force vector, where $f \in \mathbb{R}$ represents total force of the rotors.

Here, $\boldsymbol{f}_c$ and $\boldsymbol{\tau}_c$ are dynamic coupling force and torque caused by the Delta arm. They are given as [13]

$$\begin{aligned}\boldsymbol{f}_c =& -(m_B + m_M)\,\boldsymbol{R}\left[\boldsymbol{\omega}\times\left(\boldsymbol{\omega}\times\boldsymbol{p}_C^B\right)\right.\\ &\left.+\dot{\boldsymbol{\omega}}\times\boldsymbol{p}_C^B + 2\boldsymbol{\omega}\times\dot{\boldsymbol{p}}_C^B + \ddot{\boldsymbol{p}}_C^B\right],\end{aligned} \tag{7}$$

$$\begin{aligned}\boldsymbol{\tau}_c =& -\boldsymbol{M}_M^B\dot{\omega} - \boldsymbol{\omega}\times\left(\boldsymbol{M}_M^B\boldsymbol{\omega}\right) - \dot{\boldsymbol{M}}_M^B\boldsymbol{\omega}\\ &+(m_B + m_M)\boldsymbol{p}_C^B\times\boldsymbol{R}^{-1}\left(\boldsymbol{g} - \dot{\boldsymbol{v}}\right)\\ &-\frac{(m_B + m_M)^2}{m_M}\left[\boldsymbol{p}_C^B\times\ddot{\boldsymbol{p}}_C^B - \boldsymbol{\omega}\times\left(\boldsymbol{p}_C^B\times\dot{\boldsymbol{p}}_C^B\right)\right],\end{aligned} \tag{8}$$

where $\boldsymbol{p}_C^B$ is the center of mass of the aerial manipulator in Σ_B, $\boldsymbol{M}_M^B$ is the inertia matrix of the Delta arm in Σ_B. Although the expressions of $\boldsymbol{f}_c$ and $\boldsymbol{\tau}_c$ are given in (7) and (8), they cannot be measured in practice since $\dot{\boldsymbol{M}}_M^B$, $\dot{\boldsymbol{p}}_C^B$, and $\ddot{\boldsymbol{p}}_C^B$ are difficult to measure. The mass m_M and the inertia matrix $\boldsymbol{M}_M^B$ of the Delta arm are contained in model (6). In the absence of the Delta arm, we have $m_M \equiv 0$, $\boldsymbol{M}_M^B \equiv 0$, $\boldsymbol{p}_C^B \equiv 0$ and $\dot{\boldsymbol{M}}_M^B \equiv 0$. In this case, model (6) degenerates to a standard quadcopter model.

E. Extended state observer

Preliminaries of the ESO are given below. The stability analysis and other details about the ESO can be found in [29].

Consider a system with input $u \in \mathbb{R}$ and output $y \in \mathbb{R}$ in the form $y^{(n)} = \Delta + u$, where $\Delta \in \mathbb{R}$ is the unknown term of the system. The output y can be measured by sensors. Denote $y_1 = y, y_2 = \dot{y}, \cdots, y_n = y^{(n)}$. We define y_{n+1} as an extended state variable and $y_{n+1} = \Delta$. The original plant is now described as $\dot{y}_1 = y_2, \dot{y}_2 = y_3, \cdots, \dot{y}_{n-1} = y_n, \dot{y}_n = y_{n+1} + u, \dot{y}_{n+1} = \dot{\Delta}$. The purpose of the ESO is to estimate Δ by utilizing the measurable output y.

Let $\hat{y}_1, \cdots, \hat{y}_{n+1}$ denote the estimated values of $y_1, \cdots, y_{n+1}$. Then, the ESO can be designed as follows [29]:

$$\begin{aligned}\dot{\hat{y}}_1 =& \hat{y}_2 + a_1(y_1 - \hat{y}_1),\\ &\vdots\\ \dot{\hat{y}}_{n-1} =& \hat{y}_n + a_{n-1}(y_1 - \hat{y}_1),\\ \dot{\hat{y}}_n =& \hat{y}_{n+1} + a_n(y_1 - \hat{y}_1) + u,\\ \dot{\hat{y}}_{n+1} =& a_{n+1}(y_1 - \hat{y}_1),\end{aligned} \tag{9}$$

where $a_1 = w_o\alpha_1, a_2 = w_o^2\alpha_2, \cdots, a_{n+1} = w_o^{n+1}\alpha_{n+1}$, where $\alpha_i = (n+1)!/[i!(n+1-i)!], i = 1, 2, \cdots, n+1$. Let w_o denote the observer bandwidth and $w_o > 0$. Let $\tilde{y}_i = y_i - \hat{y}_i$ $(i = 1, \cdots, n+1)$ denote the estimation errors. Combining the original plant and (9), the error dynamics are given as

$$\begin{aligned}\dot{\tilde{y}}_1 =& \tilde{y}_2 - w_o\alpha_1\tilde{y}_1,\\ &\vdots\\ \dot{\tilde{y}}_n =& \tilde{y}_{n+1} - w_o^n\alpha_1\tilde{y}_1,\\ \dot{\tilde{y}}_{n+1} =& \dot{\Delta} - w_o^{n+1}\alpha_1\tilde{y}_1.\end{aligned} \tag{10}$$

According to [29], if $\dot{\Delta}$ is bounded, i.e., $|\dot{\Delta}| \le \delta$, then there exists a constant $c_i > 0$ and a finite time $T_1 > 0$ such that $|\tilde{y}_i(t)| \le c_i$ $(i = 1, \cdots, n+1)$ for all $t \ge T_1 > 0$ and $w_o > 0$. Furthermore,

$$c_i = (\tilde{y}_{sum}(0) + h_i\delta)/w_o^k, \tag{11}$$

for some positive integer k, where $\tilde{y}_{sum}(0) = |\tilde{y}_1(0)| + |\tilde{y}_2(0)| + \cdots + |\tilde{y}_{n+1}(0)|$ and h_i is constant. From (11), it can be concluded that the estimation error bound of the ESO is determined by the initial estimation error, δ, and observer bandwidth w_o. Since the unknown term Δ cannot be measured, the initial estimation error and δ cannot be utilized to reduce c_i. Gain w_o is inversely proportional to $1/c_i^k$. Then, a smaller value of c_i can be achieved by an ESO with a larger w_o.

This article has been accepted for publication in IEEE Transactions on Automation Science and Engineering. This is the author's version which has not been fully edited and content may change prior to final publication. Citation information: DOI 10.1109/TASE.2023.3260874

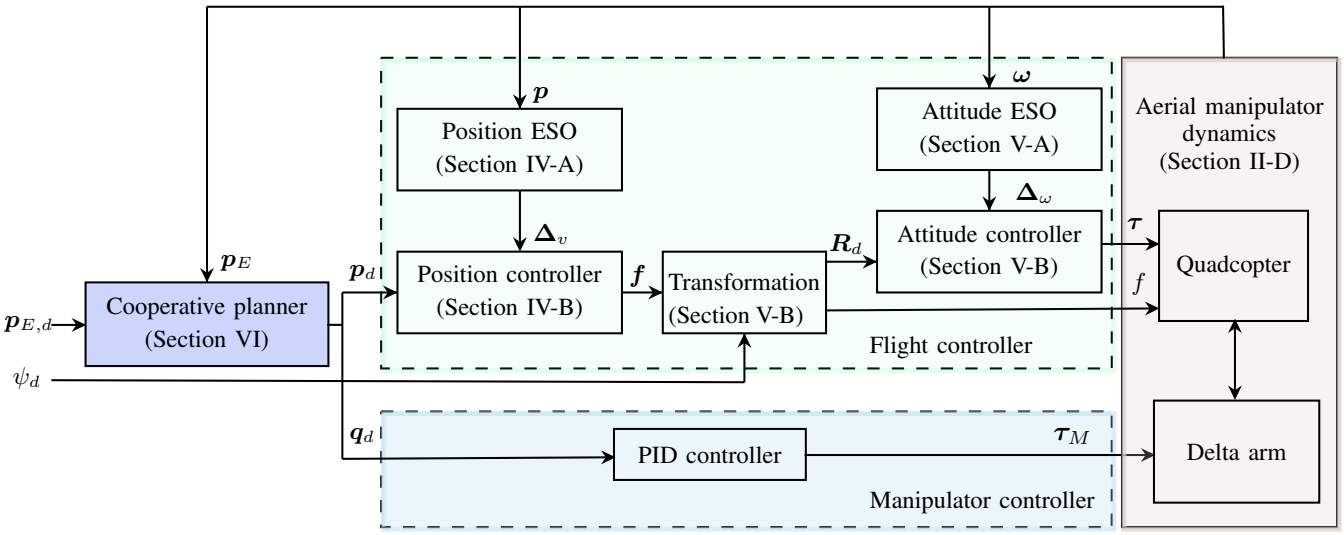

Fig. 3: The proposed control structure of the aerial manipulator system.

III. Control System Overview

The overall control system of the aerial manipulator is decomposed into three components as illustrated in Fig. 3.

The first component is the cooperative planner. Its input is the desired trajectory of the end-effector $\boldsymbol{p}_{E,d}$. Its outputs are the planned trajectories $\boldsymbol{p}_d$ and $\boldsymbol{q}_d$ for the quadcopter base and the Delta arm. The proposed planner has two modes: P-P and E-P modes, which makes the planner suitable for different scenarios. Besides, the physical constraints are considered in the planner to ensure the solution is feasible. Compared with the existing methods, the proposed planner adapts to more scenarios since it has two modes and considers the physical constraints.

The second component is the flight controller for the quadcopter base. Its input is the desired trajectory planned by the cooperative planner. Its outputs are $\boldsymbol{\tau}$ and f, which are the torque and force commands of the quadcopter. This flight controller can be further decomposed into a few subcomponents. The first is an ESO-based position controller. It aims to generate the force vector $\boldsymbol{f}$ for the quadcopter so that the desired position $\boldsymbol{p}_d$ can be tracked. The closed-loop position system converges to predesigned dynamics that are constituted by position and velocity subloops. The second is an ESO-based attitude controller. It aims to generate the torque vector command for the quadcopter so that the desired attitude $\boldsymbol{R}_d$ can be tracked. The closed-loop attitude system also converges to predesigned dynamics that are constituted by attitude and angular velocity subloops. All the corresponding sections introducing these subcomponents are listed in Fig. 3. All parameters of the flight controller are included in the predesigned dynamics and can be determined according to the performance requirement.

The third component is the Delta arm controller. Its input is the desired joint angles of the Delta arm. The output is the torques that each actuator should generate. The Delta arm controller is constituted of three actuator controllers. We use Dynamixel AX28 servomotors as the actuators of the Delta arm. The controllers of the servomotors are designed by the traditional PID method [30].

IV. Position Control of the Quadcopter Base

In this section, the position controller of the quadcopter base is designed by an ESO-based nonlinear control method. First, the coupling between the quadcopter base and the Delta arm is estimated by a position ESO. Then, the feedback linearization control method is adopted to design the position controller.

From model (6) and (7), the position dynamics can be rewritten in a compact form as

$$\begin{aligned} \dot{\boldsymbol{p}} &= \boldsymbol{v}, \\ \dot{\boldsymbol{v}} &= \boldsymbol{u}_v + \boldsymbol{\Delta}_v. \end{aligned} \tag{12}$$

where

$$\boldsymbol{u}_v = \boldsymbol{g} + \boldsymbol{a}_f - \boldsymbol{f}/(m_B + m_M) \in \mathbb{R}^3, \tag{13}$$

the coupling force is rewritten as $\boldsymbol{f}_c = (m_B + m_M)(\boldsymbol{a}_f + \boldsymbol{\Delta}_v)$, where $\boldsymbol{a}_f = -\boldsymbol{R}\boldsymbol{\omega} \times (\boldsymbol{\omega} \times \boldsymbol{p}_C^B)$ represents the first order term of $\boldsymbol{f}_c$ and can be used in controller design directly,

$$\boldsymbol{\Delta}_v = -\boldsymbol{R}(\dot{\boldsymbol{\omega}} \times \boldsymbol{p}_C^B + 2\boldsymbol{\omega} \times \dot{\boldsymbol{p}}_C^B + \ddot{\boldsymbol{p}}_C^B) \in \mathbb{R}^3 \tag{14}$$

represents the second order term of $\boldsymbol{f}_c$. $\boldsymbol{\Delta}_v$ is treated as an unknown term, because $\dot{\boldsymbol{\omega}}, \dot{\boldsymbol{p}}_C^B$ and $\ddot{\boldsymbol{p}}_C^B$ can not be sensed by the aerial manipulator.

A. Position ESO for coupling estimation

A third-order position ESO is designed to estimate unknown term $\boldsymbol{\Delta}_v$. Let $\hat{\boldsymbol{p}}, \hat{\boldsymbol{v}}, \hat{\boldsymbol{\Delta}}_v$ denote the estimates of $\boldsymbol{p}, \boldsymbol{v}, \boldsymbol{\Delta}$, respectively. According to Section II-E, the position ESO is designed as

$$\begin{aligned} \dot{\hat{p}}_i &= \hat{v}_i + 3w_{p,i}(p_i - \hat{p}_i), \\ \dot{\hat{v}}_i &= u_{v,i} + \hat{\Delta}_{v,i} + 3w_{p,i}^2(p_i - \hat{p}_i), \\ \dot{\hat{\Delta}}_{v,i} &= w_{p,i}^3(p_i - \hat{p}_i), \quad i = 1, 2, 3, \end{aligned} \tag{15}$$

This article has been accepted for publication in IEEE Transactions on Automation Science and Engineering. This is the author's version which has not been fully edited and content may change prior to final publication. Citation information: DOI 10.1109/TASE.2023.3260874

where $\hat{p}_i, \hat{v}_i, \hat{\Delta}_{v,i}$ denote the i-th elements of $\hat{\boldsymbol{p}}, \hat{\boldsymbol{v}}, \hat{\boldsymbol{\Delta}}$, respectively, $u_{v,i}$ is the i-th element of $\boldsymbol{u}_v$. In addition, $\boldsymbol{w}_p = [w_{p,1}, w_{p,2}, w_{p,3}]^T \in \mathbb{R}^3$ is the bandwidth vector of the position ESO and it can be adjusted.

According to Section II-E and (11), the estimation error is bounded, i.e., $\lim_{t\to\infty} |\Delta_{v,i} - \hat{\Delta}_{v,i}| \leq c_{p,i}, i = 1,2,3$. According to (11), $c_{p,1}, c_{p,2}, c_{p,3}$ are inversely proportional to $w_{p,1}, w_{p,2}, w_{p,3}$ to the k-th power. Then, the position ESO with the larger gain vector $\boldsymbol{w}_p$ achieves the smaller estimation error bound. Let c_p denote three times the maximum of the bounds $c_{p,1}, c_{p,2}, c_{p,3}$, i,e., $c_p = 3\max\{c_{p,1}, c_{p,2}, c_{p,3}\}$. Then, we have $\lim_{t\to\infty} \|\boldsymbol{\Delta}_v - \hat{\boldsymbol{\Delta}}_v\| \leq c_p$.

B. Nonlinear position controller

The dynamic behavior is significant for the aerial manipulator system. To control more flight modes of the quadcopter (e.g., position mode, altitude mode), the closed-loop dynamics of the position loop are divided into two subloops: position and velocity subloops. The two-subloop structure matches the cascade structure of the autopilot used in the quadcopter. Let $\boldsymbol{p}_d \in \mathbb{R}^3$ and $\tilde{\boldsymbol{p}} = \boldsymbol{p} - \boldsymbol{p}_d \in \mathbb{R}^3$ denote the desired position and the position error of the quadcopter base, respectively. The desired dynamics of the two subloops are given as

$$\dot{\tilde{\boldsymbol{p}}} + 2\boldsymbol{\Lambda}_p\tilde{\boldsymbol{p}} + \boldsymbol{\Lambda}_p^2 \int_0^t \tilde{\boldsymbol{p}}(\tau)d\tau = 0, \tag{16}$$

$$\dot{\boldsymbol{r}}_v + \boldsymbol{K}_v\boldsymbol{r} = 0, \tag{17}$$

where $\boldsymbol{\Lambda}_p \in \mathbb{R}^{3\times3}$ is a positive diagonal matrix, $\boldsymbol{K}_v \in \mathbb{R}^{3\times3}$ is a positive definite matrix. In addition, $\boldsymbol{r}_v = \boldsymbol{v} - \boldsymbol{v}_r$, where $\boldsymbol{v}_r$ is the desired velocity reference trajectory. To achieve the desired position subloop, we design $\boldsymbol{v}_r$ as

$$\boldsymbol{v}_r = \dot{\boldsymbol{p}}_d - 2\boldsymbol{\Lambda}_p\tilde{\boldsymbol{p}} - \boldsymbol{\Lambda}_p^2 \int_0^t \tilde{\boldsymbol{p}}(\tau)d\tau. \tag{18}$$

The relationship between $\boldsymbol{v}_r$ and $\dot{\boldsymbol{p}}_d$ can be shown in (18). Then, we have

$$\boldsymbol{r}_v = \dot{\tilde{\boldsymbol{p}}} + 2\boldsymbol{\Lambda}_p\tilde{\boldsymbol{p}} + \boldsymbol{\Lambda}_p^2 \int_0^t \tilde{\boldsymbol{p}}(\tau)d\tau. \tag{19}$$

From (19), one can conclude that the desired position subloop can be achieved as $\boldsymbol{r}_v \to 0$. The relationship between $\boldsymbol{r}_v$ and $\tilde{\boldsymbol{p}}$ is described in Lemma 1.

Lemma 1: Let c_1 denote a constant. If $\|\boldsymbol{r}_v\| \leq c_1$ as $t \to \infty$, then $\|\tilde{\boldsymbol{p}}\| \leq c_1 \mathrm{tr}(\boldsymbol{\Lambda}_p^{-1})$ as $t \to \infty$, where $\mathrm{tr}(\boldsymbol{\Lambda}_p^{-1})$ denotes the trace of $\boldsymbol{\Lambda}_p^{-1}$.

Proof: According to the definition of $\boldsymbol{r}_v$, we have

$$\dot{\tilde{\boldsymbol{p}}} = -2\boldsymbol{\Lambda}_p\tilde{\boldsymbol{p}} - \boldsymbol{\Lambda}_p^2 \int_0^t \tilde{\boldsymbol{p}}(\tau)d\tau + \boldsymbol{r}_v. \tag{20}$$

Let $\tilde{p}_i$ denote the i-th element of $\tilde{\boldsymbol{p}}$. Let $[\Lambda_p]_{i,j}$ denote the element in the i-th row and j-th column of $\boldsymbol{\Lambda}_p$. Then, we have

$$\dot{\boldsymbol{\eta}}_i = \underbrace{\begin{bmatrix} 0 & 1 \\ -[\Lambda_p]_{i,i}^2 & -2[\Lambda_p]_{i,i} \end{bmatrix}}_{\boldsymbol{A}_i} \boldsymbol{\eta}_i + \underbrace{\begin{bmatrix} 0 \\ s_i \end{bmatrix}}_{\boldsymbol{s}_i} \tag{21}$$

where $\boldsymbol{\eta}_i = [\int_0^t \tilde{p}_i d\tau, \tilde{p}_i]^T$, where $\boldsymbol{A}_i$ is the Hurwitz matrix and its eigenvalue is $[\Lambda_p]_{i,i}$ with multiplicity 2. According to bounded input bounded output (BIBO) stability [31, Section 5.2], we have $\|\boldsymbol{\eta}_i\| \leq c_1/[\Lambda_p]_{i,i}$ as $t \to \infty$. Under the definition of $\boldsymbol{\eta}_i$, we have $|\tilde{p}_i| \leq c_1/[\Lambda_p]_{i,i}$. Then, one can conclude that $\|\tilde{\boldsymbol{p}}\| \leq c_1 \mathrm{tr}(\boldsymbol{\Lambda}_p^{-1})$ as $t \to \infty$. □

To achieve the desired velocity subloop, the position control law is designed as

$$\boldsymbol{u}_v = -\boldsymbol{K}_v\boldsymbol{r}_v + \dot{\boldsymbol{v}}_r - \hat{\boldsymbol{\Delta}}_v. \tag{22}$$

Substituting control law (22) into (12) gives

$$\dot{\boldsymbol{r}}_v + \boldsymbol{K}_v\boldsymbol{r}_v = \boldsymbol{\Delta}_v - \hat{\boldsymbol{\Delta}}_v. \tag{23}$$

According to Section IV-A, $\|\boldsymbol{\Delta}_v - \hat{\boldsymbol{\Delta}}_v\|$ is bounded. It means that the desired velocity subloop can be achieved boundedly. Then, the control force vector $\boldsymbol{f}$ can be inferred from (13):

$$\boldsymbol{f} = (m_B + m_M)\left(\boldsymbol{g} + \boldsymbol{a}_f + \boldsymbol{K}_v\boldsymbol{r}_v - \dot{\boldsymbol{v}}_r + \hat{\boldsymbol{\Delta}}_v\right). \tag{24}$$

We now prove the stability of the position dynamics with control law (24).

Theorem 1: Assuming that $\dot{\boldsymbol{\Delta}}_v$ is bounded, i.e., $\|\dot{\boldsymbol{\Delta}}_v\| \leq \delta_v$, if the position controller is designed as (24) with position ESO (15), then the position tracking error $\tilde{\boldsymbol{p}}$ is bounded, i.e., $\|\tilde{\boldsymbol{p}}\| \leq c_p \mathrm{tr}(\boldsymbol{\Lambda}_p^{-1})/\lambda_{\min}(\boldsymbol{K}_v)$ as $t \to \infty$, where c_p is the upper bound of the estimation error from the position ESO.

Proof: Combining position control law (24) and position model (12), the error dynamics can be written as

$$\begin{aligned} \dot{\boldsymbol{r}}_v =& \boldsymbol{g} + \boldsymbol{a}_f - \boldsymbol{f}/(m_B + m_M) + \boldsymbol{\Delta}_v - \dot{\boldsymbol{v}}_r \\ =& -\boldsymbol{K}_v\boldsymbol{r}_v + \boldsymbol{\Delta}_v - \hat{\boldsymbol{\Delta}}_v. \end{aligned} \tag{25}$$

Define a Lyapunov function as

$$V(\boldsymbol{r}_v) = \frac{1}{2}\boldsymbol{r}_v^T\boldsymbol{r}_v. \tag{26}$$

With error dynamics (25), the time derivative of V is

$$\dot{V} = -\boldsymbol{r}_v^T\boldsymbol{K}_v\boldsymbol{r}_v + \boldsymbol{r}_v^T(\boldsymbol{\Delta}_v - \hat{\boldsymbol{\Delta}}_v). \tag{27}$$

According to Section IV-A, the estimation error of the position ESO (15) is bounded. The upper bound of the estimation error is represented as c_p. Then, we have $\|\boldsymbol{\Delta}_v - \hat{\boldsymbol{\Delta}}_v\| \leq c_p$ as $t > T_p$, where T_p represents a finite time. Using the comparison theorem [31, Section 9.3], we define $W = \sqrt{V} = \|\boldsymbol{r}_v\|/\sqrt{2}$. After finite time T_p, we can obtain

$$\begin{aligned} \dot{W} &= \frac{-\boldsymbol{r}_v^T\boldsymbol{K}_v\boldsymbol{r}_v + \boldsymbol{r}_v^T(\boldsymbol{\Delta}_v - \hat{\boldsymbol{\Delta}}_v)}{\sqrt{2}\|\boldsymbol{r}_v\|} \\ &\leq \frac{-\lambda_{\min}(\boldsymbol{K}_v)\|\boldsymbol{r}_v\|^2 + c_p\|\boldsymbol{r}_v\|}{\sqrt{2}\,\|\boldsymbol{r}_v\|} \\ &= -\lambda_{\min}(\boldsymbol{K}_v)W + c_p/\sqrt{2}, \end{aligned} \tag{28}$$

where $\lambda_{\min}(\boldsymbol{K}_v)$ is the minimum eigenvalue of $\boldsymbol{K}_v$. Since $\boldsymbol{K}_v$ is a positive diagonal matrix, we have $\lambda_{\min}(\boldsymbol{K}_v) > 0$.

According to the BIBO stability [31, Section 5.2], we have $|W| \leq c_p/(\sqrt{2}\lambda_{\min}(\boldsymbol{K}_v))$ as $t \to \infty$. With the definition of W, we have $\|\boldsymbol{r}_v\| \leq c_p/\lambda_{\min}(\boldsymbol{K}_v)$ as $t \to \infty$. The relationship between $\|\tilde{\boldsymbol{p}}\|$ and $\|\boldsymbol{r}_v\|$ are given in Lemma 1.

This article has been accepted for publication in IEEE Transactions on Automation Science and Engineering. This is the author's version which has not been fully edited and content may change prior to final publication. Citation information: DOI 10.1109/TASE.2023.3260874

From the relationship, we have $\|\tilde{\boldsymbol{p}}\| \leq c_p \mathrm{tr}(\boldsymbol{\Lambda}_p^{-1})/\lambda_{\min}(\boldsymbol{K}_v)$ as $t \to \infty$. □

Theorem 1 assumes that $\dot{\boldsymbol{\Delta}}_v$ is bounded. The unknown term $\boldsymbol{\Delta}_v$ is formulated as (14) and, therefore, $\dot{\boldsymbol{\Delta}}_v$ is determined by motions of the multirotor and the Delta arm. This assumption is reasonable since the motions are physically limited. The control parameters in the position controller are $\boldsymbol{\Lambda}_p$ and $\boldsymbol{K}_v$. The two parameters are contained in the desired dynamics of the two subloops. The desired dynamics (16) is expressed as a second-order system while the desired dynamics (17) is expressed as a first-order system. Therefore, the control parameters can be determined by utilizing the features of these systems and the performance requirements.

An analysis of the tracking error is given below. The upper bound of the position tracking error is proportional to c_p, $\mathrm{tr}(\boldsymbol{\Lambda}_p^{-1})$ and inversely proportional to $\lambda_{\min}(\boldsymbol{K}_v)$. As a result, the controller with the larger control gains $\boldsymbol{\Lambda}_p$ and $\boldsymbol{K}_v$ achieves the lower position tracking error bound. Another way to reduce the position tracking error bound is by reducing the estimate bound c_p. According to Section IV-A, the position ESO with the larger bandwidth vector $\boldsymbol{w}_p$ results in a lower value of c_p. Therefore, the controller with the larger gain vector $\boldsymbol{w}_p$ can achieve the lower position tracking error bound.

V. Attitude Controller of the Quadcopter Base

In this section, an attitude controller of the quadcopter base is proposed. In particular, the coupling between the quadcopter base and the Delta arm is estimated by an attitude ESO. Then, the feedback linearization control method is adopted to design the attitude controller of the quadcopter base.

From model (6) and (8), the dynamics of the attitude loop can be rewritten as

$$\begin{aligned} \dot{\boldsymbol{R}} &= \boldsymbol{R}[\boldsymbol{\omega}]_\times, \\ \dot{\boldsymbol{\omega}} &= \boldsymbol{u}_\omega + \boldsymbol{\Delta}_\omega. \end{aligned} \tag{29}$$

The first term in the second equation of (29) is a composite vector expressed as

$$\boldsymbol{u}_\omega = \boldsymbol{M}^{-1}[\boldsymbol{\tau} - \boldsymbol{\omega} \times (\boldsymbol{M}\boldsymbol{\omega}) + \boldsymbol{\tau}_s], \tag{30}$$

the coupling torque can be rewritten as $\boldsymbol{\tau}_c = \boldsymbol{\tau}_s + \boldsymbol{M}\boldsymbol{\Delta}_\omega$, where

$$\boldsymbol{\tau}_s = (m_B + m_M)\boldsymbol{p}_C^B \times \boldsymbol{R}^{-1}\boldsymbol{g} - \boldsymbol{\omega} \times \left(\boldsymbol{M}_M^B \boldsymbol{\omega}\right) \tag{31}$$

represents the first order term of $\boldsymbol{\tau}_c$ and can be used in controller design directly. The second term in the second equation of (29) represents the second order term of $\boldsymbol{\tau}_c$ and can be expressed as

$$\begin{aligned} \boldsymbol{\Delta}_\omega = -\boldsymbol{M}^{-1}\Big\{ & \boldsymbol{M}_M^B \dot{\boldsymbol{\omega}} + \dot{\boldsymbol{M}}_M^B \boldsymbol{\omega} \\ & + (m_B + m_M)\boldsymbol{p}_C^B \times \boldsymbol{R}^{-1}\dot{\boldsymbol{v}} \\ & + \frac{(m_B + m_M)^2}{m_M}\left[\boldsymbol{p}_C^B \times \ddot{\boldsymbol{p}}_C^B - \boldsymbol{\omega} \times (\boldsymbol{p}_C^B \times \dot{\boldsymbol{p}}_C^B)\right] \Big\}. \end{aligned} \tag{32}$$

By definition, the dynamic influence $\boldsymbol{\Delta}_\omega$ is a function of $\dot{\boldsymbol{\omega}}, \dot{\boldsymbol{v}}, \dot{\boldsymbol{M}}_M^B, \dot{\boldsymbol{p}}_C^B, \ddot{\boldsymbol{p}}_C^B$. We treat $\boldsymbol{\Delta}_\omega$ as an unknown term to be estimated, since $\dot{\boldsymbol{\omega}}, \dot{\boldsymbol{v}}, \dot{\boldsymbol{M}}_M^B, \dot{\boldsymbol{p}}_C^B, \ddot{\boldsymbol{p}}_C^B$ are not measurable.

A. Attitude ESO for coupling estimation

An attitude ESO is designed to estimate unknown term $\boldsymbol{\Delta}_\omega$ according to the method in Section II-E. Let $\hat{\boldsymbol{\omega}}, \hat{\boldsymbol{\Delta}}_\omega$ denote the estimates of $\boldsymbol{\omega}, \boldsymbol{\Delta}_\omega$, respectively. To estimate $\boldsymbol{\Delta}_\omega$, the attitude ESO is designed as

$$\begin{aligned} \dot{\hat{\omega}}_i &= u_{\omega,i} + \hat{\Delta}_{\omega,i} + 2w_{\omega,i}(\omega_i - \hat{\omega}_i), \\ \dot{\hat{\Delta}}_{\omega,i} &= w_{\omega,i}^2(\omega_i - \hat{\omega}_i), \quad i = 1,2,3, \end{aligned} \tag{33}$$

where $u_{\omega,i}$ is the i-th element of $\boldsymbol{u}_\omega$, $\boldsymbol{w}_\omega = [w_{\omega,1}, w_{\omega,2}, w_{\omega,3}]^T \in \mathbb{R}^3$ is the bandwidth vector of the attitude ESO and it can be adjusted, $\hat{\omega}_i, \hat{\Delta}_{\omega,i}$ denote the i-th elements of $\hat{\boldsymbol{\omega}}$ and $\hat{\boldsymbol{\Delta}}_\omega$, respectively.

According to Section II-E and (11), the estimation error is bounded, i.e., $\|\Delta_{\omega,i} - \hat{\Delta}_{\omega,i}\| \leq c_{\omega,i}, i = 1,2,3$. Besides, $c_{\omega,1}, c_{\omega,2}, c_{\omega,3}$ are inversely proportional to $w_{\omega,1}, w_{\omega,2}, w_{\omega,3}$ to the k-th power. Therefore, the attitude ESO with the larger gain vector $\boldsymbol{w}_\omega$ achieves the smaller estimation error bound. Let c_ω denote three times the maximum value of the bounds $c_{\omega,1}, c_{\omega,2}, c_{\omega,3}$, i.e., $c_p = 3\max\{c_{\omega,1}, c_{\omega,2}, c_{\omega,3}\}$. Then, we have $\lim_{t\to\infty} \|\boldsymbol{\Delta}_\omega - \hat{\boldsymbol{\Delta}}_\omega\| \leq c_\omega$.

B. Nonlinear attitude controller

Let $\boldsymbol{R}_d = [\boldsymbol{b}_1, \boldsymbol{b}_2, \boldsymbol{b}_3] \in SO(3)$ denote the desired rotation matrix of the quadcopter. We define $\boldsymbol{a} = [\cos\psi, \sin\psi, 0]^T$. Then, we have

$$f = \|\boldsymbol{f}\|, \boldsymbol{b}_3 = \frac{\boldsymbol{u}_v}{\|\boldsymbol{u}_v\|}, \boldsymbol{b}_2 = \frac{\boldsymbol{b}_3 \times \boldsymbol{a}}{\|\boldsymbol{b}_3 \times \boldsymbol{a}\|}, \boldsymbol{b}_1 = \boldsymbol{b}_2 \times \boldsymbol{b}_3. \tag{34}$$

Let $\boldsymbol{\omega}_d$ denote the desired angular velocity of the quadcopter and it can be calculated by

$$\boldsymbol{\omega}_d = [\boldsymbol{R}^T \dot{\boldsymbol{R}}_d]^\vee, \tag{35}$$

where $[\cdot]^\vee$ denotes the vee map which is the inverse operation of $[\cdot]_\times$. The error rotation matrix is defined as $\tilde{\boldsymbol{R}} = \boldsymbol{R}_d^T \boldsymbol{R}$. According to [32], the error function used in $SO(3)$ is equivalent to the vector part of error quaternion $\tilde{\boldsymbol{\beta}} = [\tilde{\beta}_0, \tilde{\boldsymbol{\beta}}_v^T]^T \in \mathbb{R}^4$ from $\tilde{\boldsymbol{R}}$ with $\tilde{\beta}_0 \geq 0$ and

$$\tilde{\beta}_0 = \frac{1}{2}\sqrt{1 + \mathrm{tr}(\tilde{\boldsymbol{R}})}, \quad \tilde{\boldsymbol{\beta}}_v = \frac{1}{4\tilde{\beta}_0}[\tilde{\boldsymbol{R}} - \tilde{\boldsymbol{R}}^T]^\vee. \tag{36}$$

Let $\dot{\tilde{\boldsymbol{R}}}$ be the derivative of the error rotation matrix. It can be obtained by

$$\dot{\tilde{\boldsymbol{R}}} = \boldsymbol{R}_d^T \dot{\boldsymbol{R}} + \dot{\boldsymbol{R}}_d^T \boldsymbol{R} = \tilde{\boldsymbol{R}}[\boldsymbol{\omega} - \tilde{\boldsymbol{R}}^T \boldsymbol{\omega}_d]_\times. \tag{37}$$

To control the flight modes of the quadcopter (e.g., stabilized mode, acro mode), the closed-loop dynamics of the attitude loop are divided into two subloops: attitude and angular velocity subloops. According to [33], the designed dynamics of the two subloops are given as

$$\boldsymbol{\omega} - \tilde{\boldsymbol{R}}^T \boldsymbol{\omega}_d + 2\boldsymbol{\Lambda}_q \tilde{\boldsymbol{\beta}}_v = 0, \tag{38}$$

$$\boldsymbol{M}\dot{\boldsymbol{r}_\omega} + \boldsymbol{K}_\omega \boldsymbol{r}_\omega + k_\beta \tilde{\boldsymbol{\beta}}_v = 0, \tag{39}$$

where $\boldsymbol{K}_\omega \in \mathbb{R}^{3\times3}$ and $\boldsymbol{\Lambda} \in \mathbb{R}^{3\times3}$ in (42) are positive diagonal matrices, $k_\beta > 0$ is a constant gain. Moreover, $\boldsymbol{r}_\omega = \boldsymbol{\omega} - \boldsymbol{\omega}_r$, where $\boldsymbol{\omega}_r$ is the desired angular velocity reference trajectory.

To achieve the desired attitude subloop, we design $\boldsymbol{\omega}_r$ as

$$\boldsymbol{\omega}_r = \tilde{\boldsymbol{R}}^T\boldsymbol{\omega}_d - 2\boldsymbol{\Lambda}_q\tilde{\boldsymbol{\beta}}_v. \tag{40}$$

Then, we have

$$\boldsymbol{r}_\omega = \boldsymbol{\omega} - \tilde{\boldsymbol{R}}^T\boldsymbol{\omega}_d + 2\boldsymbol{\Lambda}_q\tilde{\boldsymbol{\beta}}_v. \tag{41}$$

According to [33], the desired attitude subloop can be achieved as $\boldsymbol{r}_\omega \to 0$.

To achieve the desired angular velocity subloop, the attitude controller of the quadcopter base is designed as follows:

$$\boldsymbol{u}_\omega = \dot{\boldsymbol{\omega}}_r - \hat{\boldsymbol{\Delta}} - \boldsymbol{M}^{-1}\boldsymbol{K}_\omega\boldsymbol{r}_\omega - \boldsymbol{M}^{-1}k_\beta\tilde{\boldsymbol{\beta}}_v, \tag{42}$$

where

$$\begin{aligned}\dot{\boldsymbol{\omega}}_r &= \dot{\tilde{\boldsymbol{R}}}^T\boldsymbol{\omega}_d + \tilde{\boldsymbol{R}}^T\dot{\boldsymbol{\omega}}_d - 2\boldsymbol{\Lambda}_q\dot{\tilde{\boldsymbol{\beta}}}_v,\\ \dot{\tilde{\boldsymbol{\beta}}}_v &= \frac{1}{2}(\tilde{\beta}_0\boldsymbol{I}_3 + \tilde{\boldsymbol{\beta}}_{v,\times})(\boldsymbol{\omega} - \tilde{\boldsymbol{R}}^T\boldsymbol{\omega}_d),\end{aligned} \tag{43}$$

where $\boldsymbol{I}_3 \in \mathbb{R}^{3\times3}$ is the identity matrix of order 3×3. Substituting the control law (42) into (29) yields

$$\boldsymbol{M}\dot{\boldsymbol{r}}_\omega + \boldsymbol{K}_\omega\boldsymbol{r}_\omega + k_\beta\tilde{\boldsymbol{\beta}}_v = \boldsymbol{\Delta}_\omega - \hat{\boldsymbol{\Delta}}_\omega. \tag{44}$$

According to Section V-A, $\|\boldsymbol{\Delta}_\omega - \hat{\boldsymbol{\Delta}}_\omega\|$ is bounded. It means that the desired angular velocity subloop can be achieved boundedly under the control law (42). Then, the control torque vector $\boldsymbol{\tau}$ is given as

$$\boldsymbol{\tau} = \boldsymbol{M}(\dot{\boldsymbol{\omega}}_r - \hat{\boldsymbol{\Delta}}) + \boldsymbol{\omega}\times(\boldsymbol{M}\boldsymbol{\omega}) - \boldsymbol{K}_\omega\boldsymbol{r}_\omega - k_\beta\tilde{\boldsymbol{\beta}}_v - \boldsymbol{\tau}_s. \tag{45}$$

We now prove the stability of the attitude loop with control law (45).

Theorem 2: Assuming that $\dot{\boldsymbol{\Delta}}_\omega$ is bounded, i.e., $\|\dot{\boldsymbol{\Delta}}_\omega\| \le \delta_\omega$, if the attitude controller is designed as (45) with the attitude ESO (33), then the attitude tracking error is bounded, i.e., $\|\tilde{\boldsymbol{\beta}}_v(t)\| \le c_q$ as $t\to\infty$, where c_q is the upper bound of the attitude tracking error.

Proof: The Lyapunov function is set as

$$V(\boldsymbol{r}_\omega, \tilde{\boldsymbol{\beta}}_v) = \frac{1}{2}\boldsymbol{s}_\omega^T\boldsymbol{M}\boldsymbol{r}_\omega + k_\beta\tilde{\boldsymbol{\beta}}_v^T\tilde{\boldsymbol{\beta}}_v + k_\beta(\tilde{\beta}_0 - 1)^2. \tag{46}$$

Because $\tilde{\beta}_0 = \sqrt{1 - \|\tilde{\boldsymbol{\beta}}_v\|}$, the $V(\boldsymbol{r}_\omega, \tilde{\boldsymbol{\beta}}_v)$ is a function of $\boldsymbol{r}_\omega$ and $\tilde{\boldsymbol{\beta}}_v$. Then, we have

$$\frac{1}{2}k_1\|\boldsymbol{\gamma}\|^2 \le V(\boldsymbol{\gamma}) \le \frac{1}{2}k_2\|\boldsymbol{\gamma}\|^2 \tag{47}$$

where k_1 is constant and $k_1 = \min\{\lambda_{\min}(\boldsymbol{M}), 2k_\beta\}$, k_2 is constant and $k_2 = \max\{\lambda_{\max}(\boldsymbol{M}), 4k_\beta\}$, $\boldsymbol{\gamma} = [\boldsymbol{r}_\omega^T, \tilde{\boldsymbol{\beta}}^T]^T$. In addition, $\lambda_{\min}(\boldsymbol{M})$ is the minimum eigenvalue of $\boldsymbol{M}$, $\lambda_{\max}(\boldsymbol{M})$ is the maximum eigenvalue of $\boldsymbol{M}$.

Using (45), we compute the time derivative of V as

$$\begin{aligned}\dot{V} &= \boldsymbol{r}_\omega^T\boldsymbol{M}\dot{\boldsymbol{s}}_\omega + 2k_\beta\tilde{\boldsymbol{\beta}}_v^T\dot{\tilde{\boldsymbol{\beta}}}_v + 2k_\beta(\tilde{\beta}_0 - 1)\dot{\tilde{q}}_0\\ &= \boldsymbol{r}_\omega^T\boldsymbol{M}(\boldsymbol{M}^{-1}\boldsymbol{K}_\omega\boldsymbol{r}_\omega - \boldsymbol{M}^{-1}k_\beta\tilde{\boldsymbol{\beta}}_v + \boldsymbol{\Delta}_\omega - \hat{\boldsymbol{\Delta}}_\omega)\\ &\quad + 2k_\beta\tilde{\boldsymbol{\beta}}_v^T\dot{\tilde{\boldsymbol{\beta}}}_v + 2k_\beta(\tilde{\beta}_0 - 1)\dot{\tilde{q}}_0.\end{aligned} \tag{48}$$

The time derivatives of $\tilde{q}_0$ and $\tilde{\boldsymbol{\beta}}_v$ are

$$\dot{\tilde{q}}_0 = -\frac{1}{2}\tilde{\boldsymbol{\beta}}_v^T\boldsymbol{e}_\omega, \quad \dot{\tilde{\boldsymbol{\beta}}}_v = \frac{1}{2}\tilde{\beta}_0\boldsymbol{e}_\omega + \frac{1}{2}\tilde{\boldsymbol{\beta}}_{v,\times}\boldsymbol{e}_\omega, \tag{49}$$

where $\boldsymbol{e}_\omega = \boldsymbol{\omega} - \tilde{\boldsymbol{R}}^T\boldsymbol{\omega}_d$. Substituting (49) into (48) yields

$$\dot{V} = -\boldsymbol{r}_\omega^T\boldsymbol{K}_\omega\boldsymbol{r}_\omega - 2k_\beta\tilde{\boldsymbol{\beta}}_v^T\boldsymbol{\Lambda}_q\tilde{\boldsymbol{\beta}}_v + \boldsymbol{r}_\omega^T\boldsymbol{M}(\boldsymbol{\Delta}_\omega - \hat{\boldsymbol{\Delta}}_\omega). \tag{50}$$

Because $\boldsymbol{\omega}_\omega$ is a positive constant vector, we have $\|\boldsymbol{\Delta}_\omega - \hat{\boldsymbol{\Delta}}_\omega\| \le c_\omega$ as $\forall t \ge T_\omega$. Then, we have

$$\dot{V} \le -k_3\|\boldsymbol{\gamma}\|^2 + \|\boldsymbol{\gamma}\|\lambda_{\min}(\boldsymbol{M})c_\omega, \quad t \ge T_\omega, \tag{51}$$

where $k_3 = \max\{\lambda_{\min}(\boldsymbol{K}_\omega), 2k_\beta\lambda_{\min}(\boldsymbol{\Lambda}_q)\}$. In addition, $\lambda_{\min}(\boldsymbol{K}_\omega)$ is the minimum eigenvalue of $\boldsymbol{K}_\omega$, $\lambda_{\min}(\boldsymbol{\Lambda}_q)$ is the minimum eigenvalue of $\boldsymbol{\Lambda}_q$.

Using (47), we have

$$-k_3\|\boldsymbol{\gamma}\|^2 \le -\frac{2k_3}{k_2}V, \quad \|\boldsymbol{\gamma}\| \le \sqrt{\frac{2V_\omega}{k_1}}. \tag{52}$$

According to the comparison theorem [31, Section 9.3], we define $W = \sqrt{V}$. Combining (51) and (52), we have

$$\begin{aligned}\dot{W} &\le -\frac{k_3}{k_2}W + \sqrt{\frac{1}{2k_1}}\lambda_{\min}(\boldsymbol{M})c_\omega\\ &= -\frac{k_3}{k_2}W + k_4,\end{aligned} \tag{53}$$

where $k_4 = \lambda_{\min}(\boldsymbol{M})c_\omega/\sqrt{2k_1}$. According to the BIBO stability [31, Section 5.2], we have $|W| \le k_2k_4/(k_3)$ as $t\to\infty$. Under the definition of W, we have $\|\boldsymbol{\gamma}\| \le \sqrt{2}W \le \sqrt{2}k_2k_4/k_3$ as $t\to\infty$. By definition of $\|\tilde{\boldsymbol{\beta}}_v\|$, we have

$$\|\tilde{\boldsymbol{\beta}}_v(t)\| \le \|\boldsymbol{\gamma}(t)\| \le c_q = \sqrt{2}k_2k_4/k_3 \tag{54}$$

as $t\to\infty$. □

From Theorem 2, one can conclude that the attitude tracking error is bounded, i.e., $\|\tilde{\boldsymbol{\beta}}_v(t)\| \le c_q$ as $t\to\infty$. An analysis of the tracking error is given below. By definitions of k_1, k_2, k_3, and k_4, (54) can be rewritten as

$$c_q = \frac{k_2\lambda_{\min}(\boldsymbol{M})c_\omega}{\sqrt{k_1}\max\{\lambda_{\min}(\boldsymbol{K}_\omega), 2k_\beta\lambda_{\min}(\boldsymbol{\Lambda}_q)\}}, \tag{55}$$

where

$$\frac{k_2}{\sqrt{k_1}} = \frac{\max\{\lambda_{\max}(\boldsymbol{M}), 4k_\beta\}}{\sqrt{\min\{\lambda_{\min}(\boldsymbol{M}), 2k_\beta\}}}. \tag{56}$$

Then, we can conclude that the upper bound of the attitude tracking error is determined by $\boldsymbol{K}_\omega, k_\beta, \lambda_{\min}(\boldsymbol{\Lambda}_q)$, and c_ω. The control gain $\boldsymbol{K}_\omega, k_\beta$, and $\lambda_{\min}(\boldsymbol{\Lambda}_q)$ are inversely proportional to upper bound c_q. As a result, the controller with the larger control gains achieves the lower attitude tracking error bound. Another way to reduce the estimation error of the attitude ESO is by reducing the estimate bound c_q, since the estimation error bound is proportional to c_q. According to Section V-A, the attitude ESO with the larger bandwidth vector $\boldsymbol{w}_\omega$ obtains a lower value of c_ω. Therefore, the controller with the larger gain vector $\boldsymbol{w}_\omega$ can achieve the lower attitude tracking error bound.

This article has been accepted for publication in IEEE Transactions on Automation Science and Engineering. This is the author's version which has not been fully edited and content may change prior to final publication. Citation information: DOI 10.1109/TASE.2023.3260874

VI. Cooperative Planning

In this section, we design a cooperative planner for the aerial manipulator. The relationship between the motion controller and the cooperative planner is described in Section III. The references of the motion controller are calculated by the cooperative planner with the given end-effector trajectory. The motion controller tracks the result references.

The physical constraints affect the feasibility of the planner. The obtained solution may violate such constraints, resulting infeasible results for the robot without considering the physical constraints. Therefore, the physical constraints of the aerial manipulator are considered in the cooperative planning. With the constraints, a planner with two modes is designed to coordinate the motions of the quadcopter and the multirotor. The two modes adapt to different scenarios.

A. Physical constraints

The physical constraints of the aerial manipulator consist of position, velocity, and acceleration constraints and can be written as

$$\boldsymbol{s}_{\min} \leq \boldsymbol{s} \leq \boldsymbol{s}_{\max}, \tag{57}$$

$$\dot{\boldsymbol{s}}_{\min} \leq \dot{\boldsymbol{s}} \leq \dot{\boldsymbol{s}}_{\max}, \tag{58}$$

$$\ddot{\boldsymbol{s}}_{\min} \leq \ddot{\boldsymbol{s}} \leq \ddot{\boldsymbol{s}}_{\max}, \tag{59}$$

where $\boldsymbol{s} = [\boldsymbol{p}^T, \boldsymbol{p}_E^{D,T}]^T$ consists of the position of the quadcopter base in Σ_I and the position of the end-effector in Σ_D, $[\cdot]_{\min}$ denotes the lower bound of the corresponding variable, and $[\cdot]_{\max}$ denotes the upper bound.

These constraints are expressed in terms of $\boldsymbol{s}, \dot{\boldsymbol{s}}, \ddot{\boldsymbol{s}}$, respectively. Using these expressions will introduce 18 variables in solving the cooperative problem. To reduce the number of variables, we convert the constraints of $\boldsymbol{s}, \ddot{\boldsymbol{s}}$ to those of $\dot{\boldsymbol{s}}$. Then, the number of the variables in solving the cooperative problem is reduced to 6.

Lemma 2: The physical constraints (57)-(59) can be approximated as

$$\underline{\dot{\boldsymbol{s}}} \leq \dot{\boldsymbol{s}} \leq \overline{\dot{\boldsymbol{s}}}, \tag{60}$$

where $\underline{\dot{\boldsymbol{s}}} = \max\{\boldsymbol{s}_{\underline{p}}, \dot{\boldsymbol{s}}_{\min}, \dot{\boldsymbol{s}}_{\underline{v}}\}$ and $\overline{\dot{\boldsymbol{s}}} = \min\{\boldsymbol{s}_{\overline{p}}, \dot{\boldsymbol{s}}_{\max}, \dot{\boldsymbol{s}}_{\overline{v}}\}$. In addition, $\boldsymbol{s}_{\underline{p}}$ and $\boldsymbol{s}_{\overline{p}}$ are lower and upper approximate bounds of the actuated state position and can be calculated by (62). $\dot{\boldsymbol{s}}_{\min}$ and $\dot{\boldsymbol{s}}_{\max}$ can be determined by (58). $\dot{\boldsymbol{s}}_{\underline{v}}$ and $\dot{\boldsymbol{s}}_{\overline{v}}$ are lower and upper approximate bounds of the actuated state acceleration and can be calculated by (66).

Proof: First, the position constraint is now converted to the constraint of $\dot{\boldsymbol{s}}$. Let Δt denote the sampling time. The actuated state in the next time step is defined as $\boldsymbol{s}_{\text{next}} \in \mathbb{R}^6$. According to the position constraint, $\boldsymbol{s}_{\text{next}}$ should satisfy the position constraint, i.e.,

$$\boldsymbol{s}_{\min} \leq \boldsymbol{s}_{\text{next}} = \boldsymbol{s} + \Delta t \dot{\boldsymbol{s}} \leq \boldsymbol{s}_{\max}. \tag{61}$$

Then, the position constraint (61) can be rewritten as

$$\boldsymbol{s}_{\underline{p}} \triangleq \frac{\boldsymbol{s}_{\min} - \boldsymbol{s}}{\Delta t} \leq \dot{\boldsymbol{s}} \leq \frac{\boldsymbol{s}_{\max} - \boldsymbol{s}}{\Delta t} \triangleq \boldsymbol{s}_{\overline{p}}. \tag{62}$$

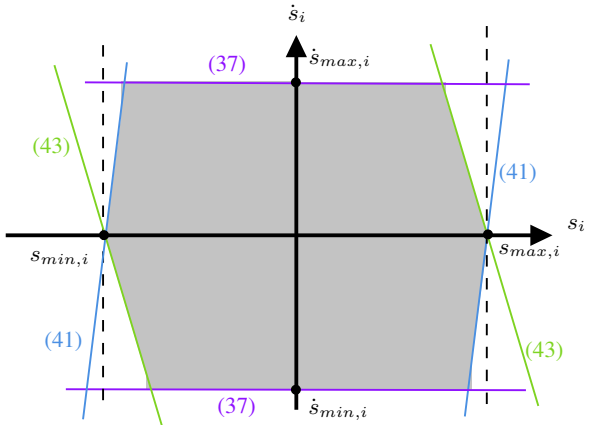

Fig. 4: The approximate physical condition. Blue line: approximate position constraint (62). Purple line: velocity constraint (58). Green line: approximate condition (64). Gray area: feasible area (60).

Second, we introduce the viability condition to handle the acceleration constraint [34]. Let s_i denote the i-th element of $\boldsymbol{s}$. Then, the viability condition is expressed as

$$\begin{aligned} s_i - \frac{\dot{s}_i^2}{2\ddot{s}_{\min,i}} - s_{\max,i} \leq 0, \\ s_i - \frac{\dot{s}_i^2}{2\ddot{s}_{\max,i}} - s_{\min,i} \geq 0, \end{aligned} \tag{63}$$

where $\ddot{s}_{\min,i}, \ddot{s}_{\max,i}, s_{\min,i}, s_{\max,i}$ denote the i-th elements of $\ddot{\boldsymbol{s}}_{\min}, \ddot{\boldsymbol{s}}_{\max}, \boldsymbol{s}_{\min}, \boldsymbol{s}_{\max}$, respectively. However, the viability condition (63) is nonlinear. We linearise the viability condition by lines passing through the two terminal points of the curves in (63). For instance, the curve of the first equation in (63) passes through $(s_i = s_{i,\max}, \dot{s}_i = 0)$ and $(s_i = s_{\max,i} + \dot{s}^2_{\max,i}/(2\ddot{s}_m), \dot{s}_i = \dot{s}_{\max,i})$. We can use a line passing through the two points to linearise the viability condition. Then the viability condition (63) is linearised as

$$\begin{aligned} \dot{s}_i - 2\frac{\ddot{s}_{\min,i}}{\dot{s}_{\max,i}} s_i + 2\frac{\ddot{s}_{\min,i}}{\dot{s}_{\max,i}} s_{\max,i} \leq 0, \\ \dot{s}_i - 2\frac{\ddot{s}_{\max,i}}{\dot{s}_{\min,i}} s_i + 2\frac{\ddot{s}_{\max,i}}{\dot{s}_{\min,i}} s_{\min,i} \geq 0. \end{aligned} \tag{64}$$

From (64), we have

$$\dot{\boldsymbol{s}}_{\underline{v}} \leq \dot{\boldsymbol{s}} \leq \dot{\boldsymbol{s}}_{\overline{v}}, \tag{65}$$

where $\dot{\boldsymbol{s}}_{\underline{v}} \in \mathbb{R}^6, \dot{\boldsymbol{s}}_{\overline{v}} \in \mathbb{R}^6$ are the lower and upper bound of the viability condition, $\dot{s}_{\underline{v},i}, \dot{s}_{\overline{v},i}$ respectively represent the i-th element of $\dot{\boldsymbol{s}}_{\underline{v}}$ and $\dot{\boldsymbol{s}}_{\overline{v}}$,

$$\begin{aligned} \dot{s}_{\underline{v},i} =& 2\frac{\ddot{s}_{\max,i}}{\dot{s}_{\min,i}} s_i - 2\frac{\ddot{s}_{\max,i}}{\dot{s}_{\min,i}} s_{\min,i}, \\ \dot{s}_{\overline{v},i} =& 2\frac{\ddot{s}_{\min,i}}{\dot{s}_{\max,i}} s_i - 2\frac{\ddot{s}_{\min,i}}{\dot{s}_{\max,i}} s_{\max,i}. \end{aligned} \tag{66}$$

The relationships among the approximate position constraint, velocity constraint, and approximation condition are illustrated in Fig. 4. □

This article has been accepted for publication in IEEE Transactions on Automation Science and Engineering. This is the author's version which has not been fully edited and content may change prior to final publication. Citation information: DOI 10.1109/TASE.2023.3260874

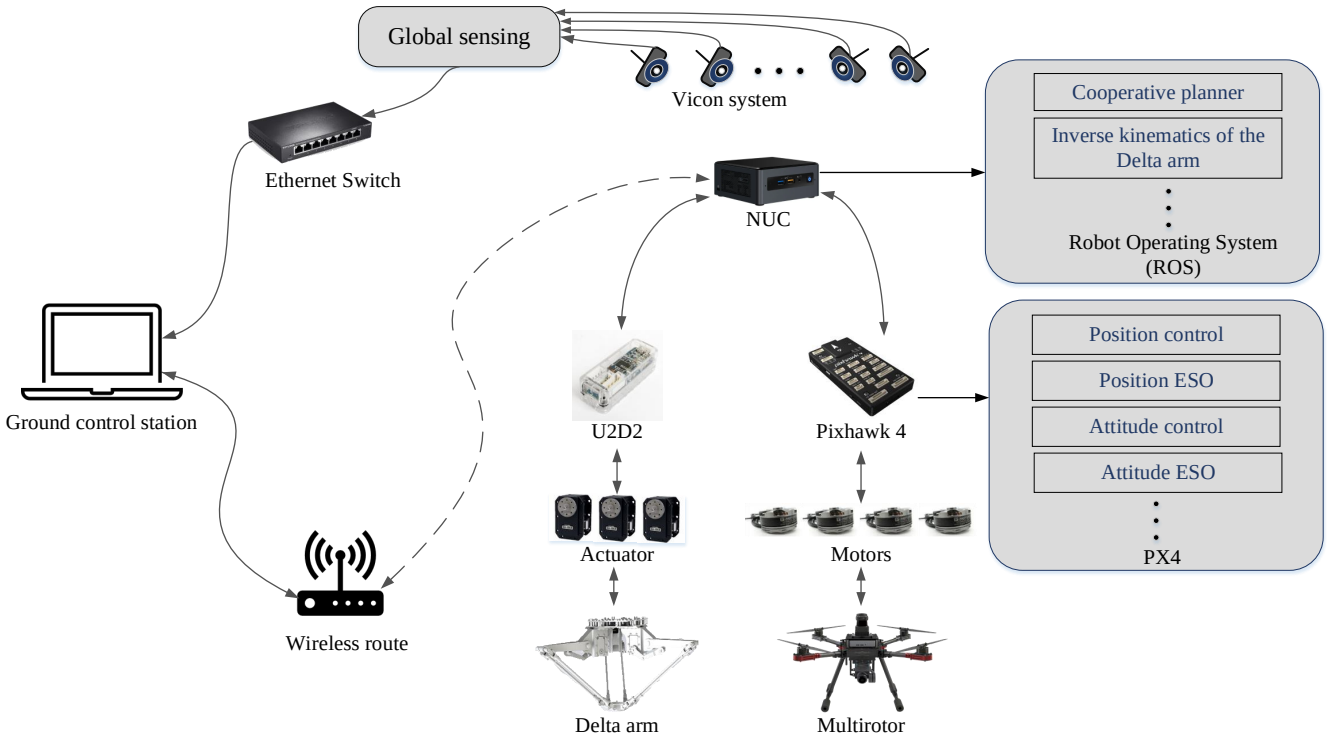

Fig. 5: Experimental setup for the aerial manipulator.

B. Cooperative method

The proposed planner provides two modes: End-effector position-Quadcopter position (P-P) and End-effector position (E-P) modes. The P-P mode steers the Delta arm and the quadcopter base with the references of the end-effector and the quadcopter, respectively. The E-P mode steers the Delta arm and the quadcopter base only with the reference of the end-effector. The P-P mode uses the quadcopter base for large-scale movements and the Delta arm for compensating for the tracking error of the end-effector. It performs better in tracking errors due to the less relative motion. However, the manipulation area of the P-P mode is small since the size of the Delta arm's workspace is limited. Compared with the P-P mode, the E-P mode has a large size of manipulation area while suffers more influence from dynamic couplings. The two modes are applicable to different scenarios. The P-P mode is applicable to pick-and-place task [22], peg-in-hole task, aerial repair task [23], etc. The E-P mode is applicable to trajectory tracking task, pulling/pushing task, etc.

1) P-P mode: The inputs of the P-P mode are desired positions of the end-effector and the quadcopter base. From (4), we obtain

$$\boldsymbol{R}\boldsymbol{R}_D^B\dot{\boldsymbol{p}}_E^D = \dot{\boldsymbol{p}}_E - \dot{\boldsymbol{p}} + [\boldsymbol{R}\boldsymbol{p}_E^B]_\times\boldsymbol{\omega}. \tag{67}$$

Inspired by the CLIK method [19, Section VA], the desired end-effector velocity in the Delta arm frame Σ_D is designed as

$$\begin{aligned}\dot{\boldsymbol{p}}_{E,\mathrm{CLIK}}^D =&(\boldsymbol{R}\boldsymbol{R}_D^B)^T[\dot{\boldsymbol{p}}_{E,d} - \boldsymbol{K}_c(\boldsymbol{p}_E - \boldsymbol{p}_{E,d})\\ &- \dot{\boldsymbol{p}} + [\boldsymbol{R}\boldsymbol{p}_E^B]_\times\boldsymbol{\omega}],\end{aligned} \tag{68}$$

where $\boldsymbol{p}_{E,d} \in \mathbb{R}^3$ is the desired end-effector position, $\dot{\boldsymbol{p}}_{E,d} \in \mathbb{R}^3$ is the desired velocity of the end-effector, $\boldsymbol{K}_c \in \mathbb{R}^{3\times3}$ is a positive diagonal matrix.

We then introduce the physical constraints of the aerial manipulator into the P-P mode. Let $\underline{\dot{\boldsymbol{p}}}_E^D$ and $\overline{\dot{\boldsymbol{p}}}_E^D$ denote the vectors that consist of the last three elements of $\underline{\dot{\boldsymbol{s}}}$ and $\overline{\dot{\boldsymbol{s}}}$. Then, we have

$$\dot{\boldsymbol{p}}_{E,d}^B = \begin{cases} \underline{\dot{\boldsymbol{p}}}_E^D, & \text{if } \dot{\boldsymbol{p}}_{E,\mathrm{CLIK}}^D < \underline{\dot{\boldsymbol{p}}}_E^D \\ \dot{\boldsymbol{p}}_{E,\mathrm{CLIK}}^D, & \text{if } \underline{\dot{\boldsymbol{p}}}_E^D < \dot{\boldsymbol{p}}_{E,\mathrm{CLIK}}^D < \overline{\dot{\boldsymbol{p}}}_E^D, \\ \overline{\dot{\boldsymbol{p}}}_E^D, & \text{if } \dot{\boldsymbol{p}}_{E,\mathrm{CLIK}}^D > \overline{\dot{\boldsymbol{p}}}_E^D. \end{cases} \tag{69}$$

Thus, the desired end-effector position in Σ_D can be obtained by integrating $\dot{\boldsymbol{p}}_{E,d}^D$. The desired actuated joint vector $\boldsymbol{q}_d$ can be obtained by the inverse kinematics of the Delta arm with $\boldsymbol{p}_{E,d}^D$ from (69).

2) E-P mode: To calculate the references of the quadcopter base and the Delta arm with the given desired end-effector position, the cooperative problem is mathematically formulated as a QP problem:

$$\begin{aligned} \min_{\dot{\boldsymbol{s}}} \quad & F(\dot{\boldsymbol{s}}) = \frac{1}{2}\dot{\boldsymbol{s}}^T\boldsymbol{W}\dot{\boldsymbol{s}} \\ \text{subject to} \quad & \boldsymbol{J}\dot{\boldsymbol{s}} = \boldsymbol{s}_c, \\ & \underline{\dot{\boldsymbol{s}}} \le \dot{\boldsymbol{s}} \le \overline{\dot{\boldsymbol{s}}}, \end{aligned} \tag{70}$$

whre $F(\dot{\boldsymbol{s}})$ is the cost function of the QP problem, $\boldsymbol{W}$ is a positive diagonal matrix, $\boldsymbol{J}$ is the actuated Jacobian matrix, $\boldsymbol{s}_c$ is a feedback inspired by the CLIK algorithm in [19, Section VA] and designed as

$$\boldsymbol{s}_c = \dot{\boldsymbol{p}}_{E,d} - \boldsymbol{K}_c(\boldsymbol{p}_E - \boldsymbol{p}_{E,d}) + [\boldsymbol{R}\boldsymbol{p}_E^B]_\times\boldsymbol{\omega}. \tag{71}$$

This article has been accepted for publication in IEEE Transactions on Automation Science and Engineering. This is the author's version which has not been fully edited and content may change prior to final publication. Citation information: DOI 10.1109/TASE.2023.3260874

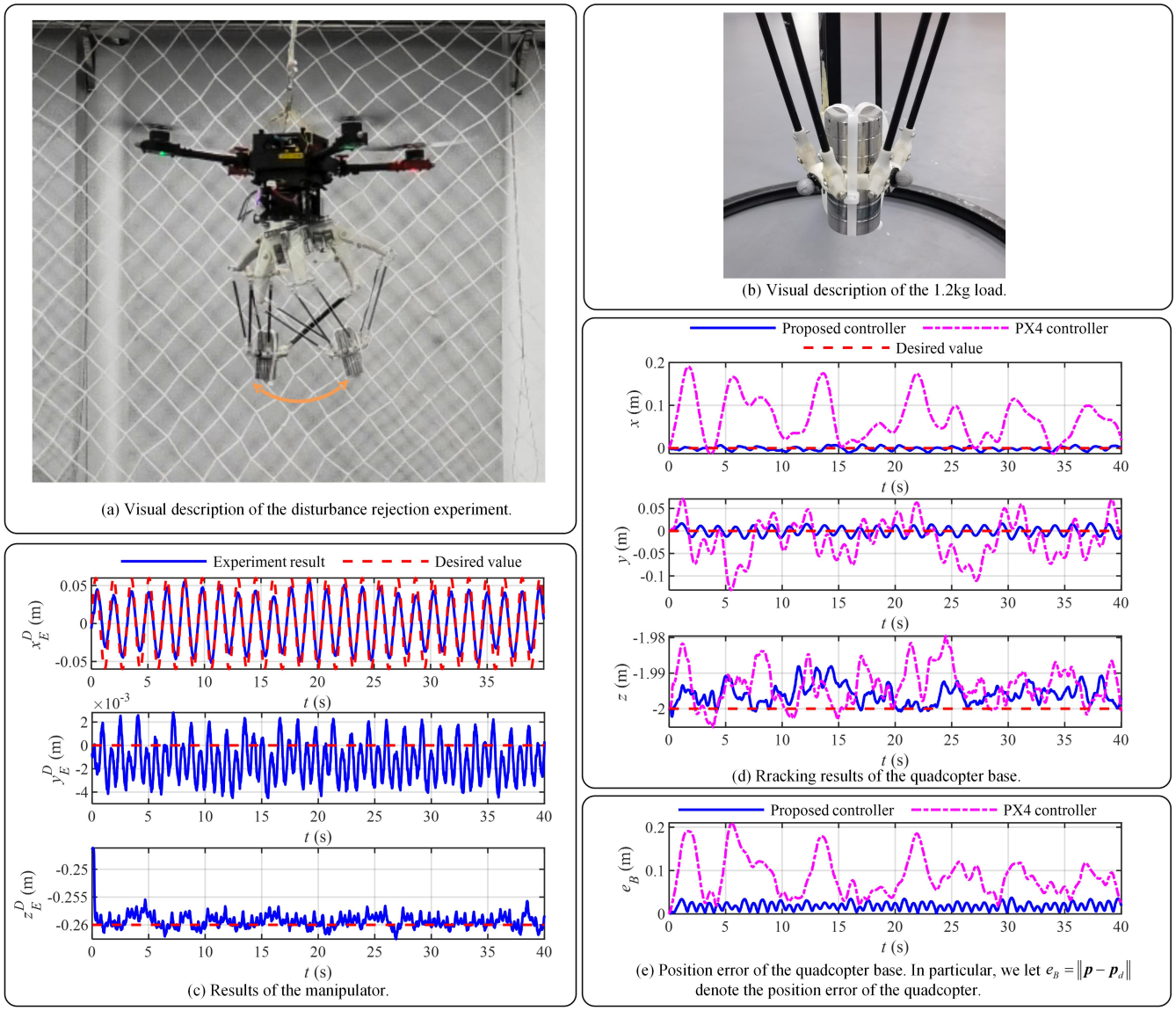

Fig. 6: Experiment results of the disturbance rejection example.

Let $\dot{\boldsymbol{s}}^* \in \mathbb{R}^6$ denote the optimal solution of QP problem (70). The constraints in (70) ensure the optimal solution $\dot{\boldsymbol{s}}^*$ to satisfy the physical constraints of the aerial manipulator. Let $\boldsymbol{s}_d = [\boldsymbol{p}_d^T, \boldsymbol{p}_{E,d}^{D,T}]^T \in \mathbb{R}^6$ denote the desired actuated state vector of the aerial manipulator. Let $\dot{\boldsymbol{s}}_d = \dot{\boldsymbol{s}}^*$ and the desired actuated state vector $\boldsymbol{s}_d$ can be obtained by integrating $\dot{\boldsymbol{s}}_d$. Then, $\boldsymbol{p}_d$ and $\boldsymbol{p}_{E,d}^D$ can be obtained from $\boldsymbol{s}_d$. From Section II-B, the desired joint vector $\boldsymbol{q}_d$ can be calculated by the inverse kinematics of the Delta arm.

The cost function shows the constraints on the energy of the cooperative planning. The weight matrix $\boldsymbol{W}$ also reflects the priority of the actuated DOFs. A smaller diagonal element means a higher priority. Therefore, we define $\boldsymbol{W}$ as follows:

$$\boldsymbol{W} = \mathrm{diag}([w_u \dot{s}_{1,M}^{-2}, w_u \dot{s}_{2,M}^{-2}, w_u \dot{s}_{3,M}^{-2}, \dot{s}_{4,M}^{-2}, \dot{s}_{5,M}^{-2}, \dot{s}_{6,M}^{-2}]), \tag{72}$$

where $w_u > 0$ is the weighting coefficient to determine the priorities of the quadcopter base and the Delta arm. w_u with a small value means the Delta arm has a higher priority. w_u with a large value means the Delta arm has a lower priority.

VII. Experimental Verification

This section presents experimental results to verify the effectiveness of the proposed algorithms. The experimental video is available at https://youtu.be/QMjGtBCUi-E.

First of all, we describe the experimental setup (see Fig. 5). The aerial manipulator platform used in the experiments consists of a quadcopter and a Delta arm. The wheelbase of the quadcopter is 0.65 m. The mass of the quadcopter (including a battery) is 3.60 kg. The Delta arm consists of a mounting base (0.56 kg) and a movable robotic arm (0.44 kg). The ESO-based flight controller runs on a Pixhawk 4 autopilot. The cooperative planner and the inverse kinematics of the Delta arm run on an onboard Intel NUC i7 computer with ROS (an open-source robotics middleware suite). The experiments are conducted in a Vicon system, which provides

This article has been accepted for publication in IEEE Transactions on Automation Science and Engineering. This is the author's version which has not been fully edited and content may change prior to final publication. Citation information: DOI 10.1109/TASE.2023.3260874

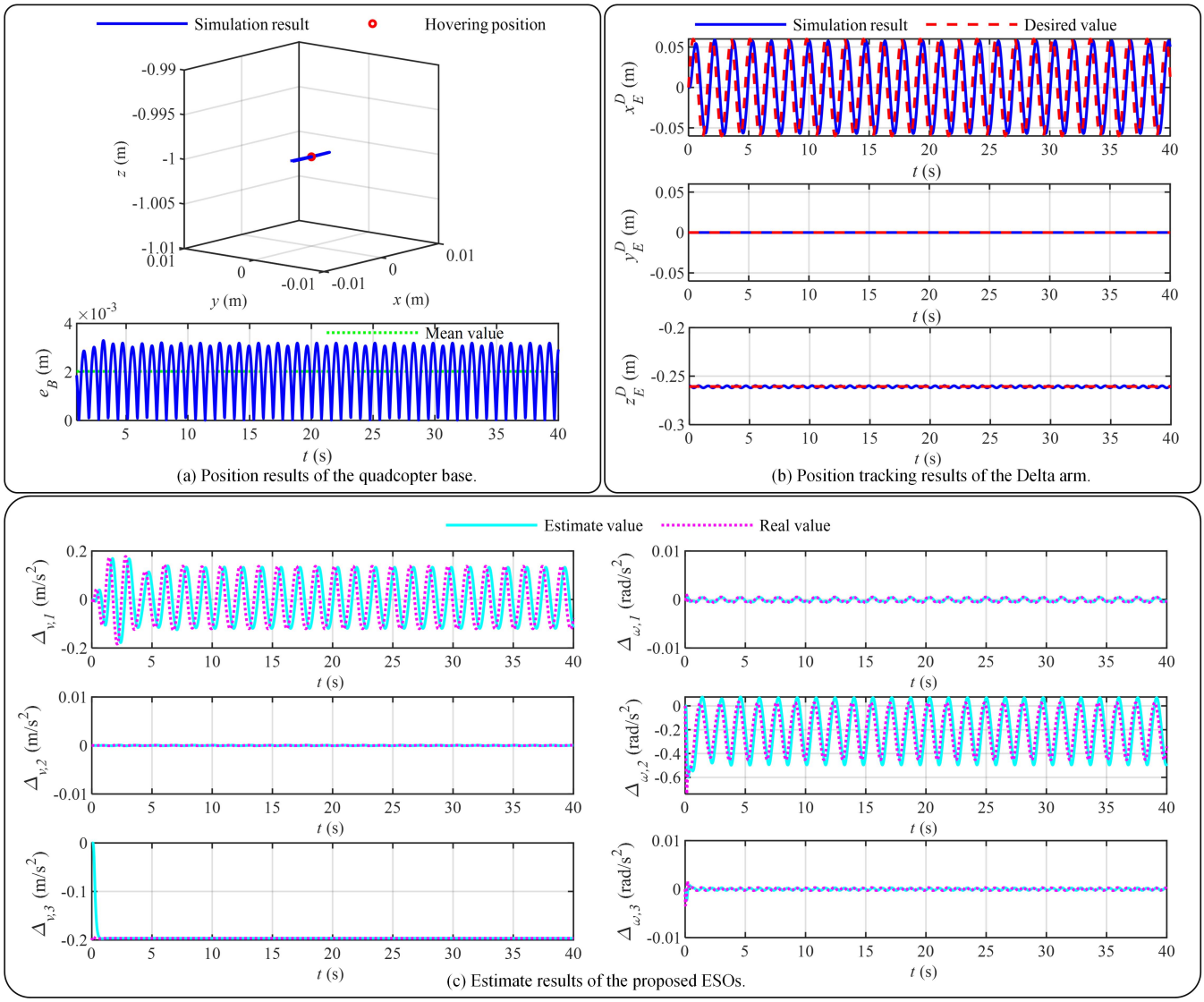

(a) Position results of the quadcopter base.

(b) Position tracking results of the Delta arm.

(c) Estimate results of the proposed ESOs.

Fig. 7: Simulation results of the disturbance rejection example.

accurate position measurements of the quadcopter base and the end-effector. The measurement data of the Vicon system is sent to a ground control station through an ethernet switch. A 5 GHz wireless router is used to connect the ground control station and the aerial manipulator. The ground control station sends the measurement data and the control command to the aerial manipulator with a frequency of 100 Hz. The aerial manipulator sends the state data to the ground control station with a frequency of 50 Hz.

In all the experiments, we use the same set of control gains: $\boldsymbol{\Lambda}_p = \text{diag}([1.5, 1.5, 1.5])$, $\boldsymbol{K}_v = \text{diag}([2.0, 2.0, 2.0])$, $\boldsymbol{\Lambda}_q = \text{diag}([3.0, 3.0, 3.0])$, $\boldsymbol{K}_\omega = \text{diag}([3.4, 3.4, 3.4])$, $k_q = 8$. The parameters of the cooperative planner are selected as $\boldsymbol{K}_c = \text{diag}([1.2, 1.2, 1.2])$, $w_u = 0.2$. The physical constraints of the aerial manipulator are given in Table II.

TABLE II: Physical constraints of the aerial manipulator.

$\boldsymbol{s}_{\min}$	$[-2, -2, -2.80, -0.08, -0.08, -0.30]^T$
$\boldsymbol{s}_{\max}$	$[2, 2, 0, 0.08, 0.08, -0.15]^T$
$\dot{\boldsymbol{s}}_{\min}$	$[-0.5, -0.5, -0.5, -0.8, -0.8, -0.8]^T$
$\dot{\boldsymbol{s}}_{\max}$	$[0.5, 0.5, 0.5, 0.8, 0.8, 0.8]^T$
$\ddot{\boldsymbol{s}}_{\min}$	$[-1, -1, -1, -2, -2, -2]^T$
$\ddot{\boldsymbol{s}}_{\max}$	$[1, 1, 1, 2, 2, 2]^T$

A. Example 1: Disturbance rejection

In the first experiment, a payload of 1.2 kg is mounted at the end of the Delta arm (Fig. 6(b)). The control objective is to maintain the position of the quadcopter base unchanged while the payload swings fast (Fig. 6(a) and (c)). Fig. 6(c) shows the tracking performance of the Delta arm. In particular, the reference of x_E^D is a sinusoidal signal with the period as 0.5π s. Since it is mechanical control, the tracking error is maintained on the level of 10^{-3} m.

The purpose of this experiment is to verify the effectiveness of the ESO and the flight controller. A PX4 1.9.0 controller is selected as a baseline for comparison. The PX4 controller has been widely used in the motion control of the

This article has been accepted for publication in IEEE Transactions on Automation Science and Engineering. This is the author's version which has not been fully edited and content may change prior to final publication. Citation information: DOI 10.1109/TASE.2023.3260874

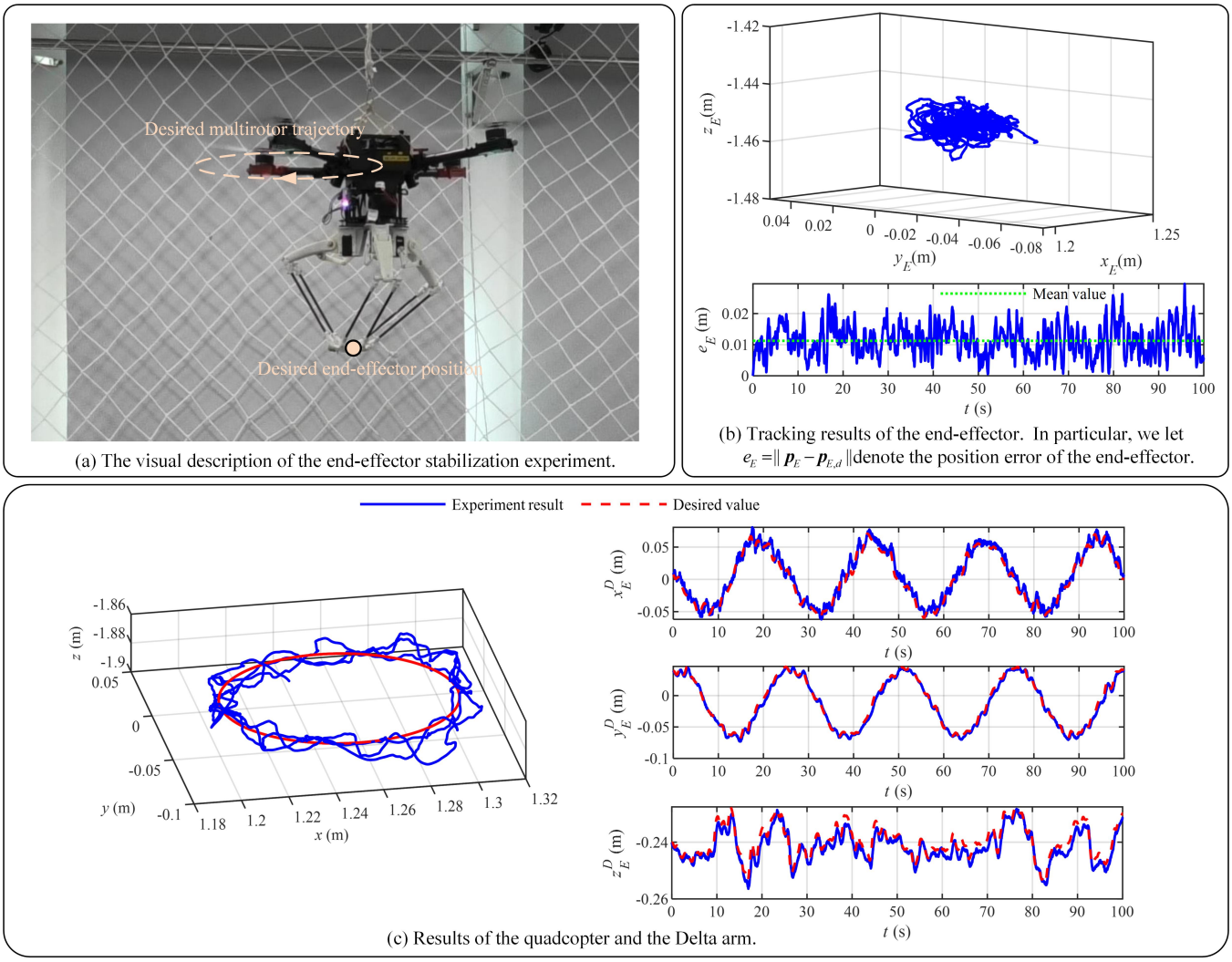

(a) The visual description of the end-effector stabilization experiment.

(b) Tracking results of the end-effector. In particular, we let $e_E = \| \boldsymbol{p}_E - \boldsymbol{p}_{E,d} \|$denote the position error of the end-effector.

(c) Results of the quadcopter and the Delta arm.

Fig. 8: Results of the end-effector stabilization experiment.

aerial manipulator [35]–[37].

Fig. 6(d)-(e) shows the position tracking performances of the proposed controller and the PX4 controller. As can be seen in Fig. 6(e), with the proposed controller, the mean position error of the quadcopter base is 0.02 m and the maximum position error reaches 0.04 m. As a comparison, with the PX4 controller, the mean position error of the quadcopter base is 0.09 m and the maximum position error reaches 0.20 m. Compared to the PX4 controller, our proposed controller can reduce the mean and maximum position errors by 78% and 80%, respectively.

In addition to the experiment on the real platform, we also conducted a simulation to verify the effectiveness of the proposed ESOs. The reason that we conduct simulation experiments is that the ground truth of the disturbances generated by the swing payload is unknown in real experiments but can be known in simulation. The simulation is conducted in Matlab Simscape without considering the noise of the aerial manipulator, a mechanical system simulation environment. The reference of the end-effector in the simulation is the same as that in the real experiment (Fig. 7(b)).

As shown in Fig. 7(a), the mean position error of the quadcopter base achieved by the proposed controller is 0.002 m, which is $1/10$ of the mean error in the real experiment. It is, however, not surprising because the real experiment is more challenging than the simulation due to various uncertainties. More importantly, Fig. 7(c) shows the estimation results of the position and the attitude ESOs. The true values of the dynamic coupling terms are calculated from (12) and (29). As can be seen, the proposed ESOs can well track the dynamic coupling terms though there is a phase delay of about 0.18 s. The good performance of the ESOs underpins the overall performance of the ESO-based controller.

To further verify the robustness of the proposed method, we conducted Monte-Carlo simulation. The simulation considers measurement noises and inertia uncertainties. The details of the noises and the uncertainties are given in Table III. In particular, we consider three cases for the ranges of the uncertainties: $\pm 5\%$, $\pm 10\%$, and $\pm 20\%$ of the corresponding nominal values. The three cases are referred to as low, middle, and high uncertainties, respectively. One thousand times of stochastic simulation were conducted for each level

This article has been accepted for publication in IEEE Transactions on Automation Science and Engineering. This is the author's version which has not been fully edited and content may change prior to final publication. Citation information: DOI 10.1109/TASE.2023.3260874

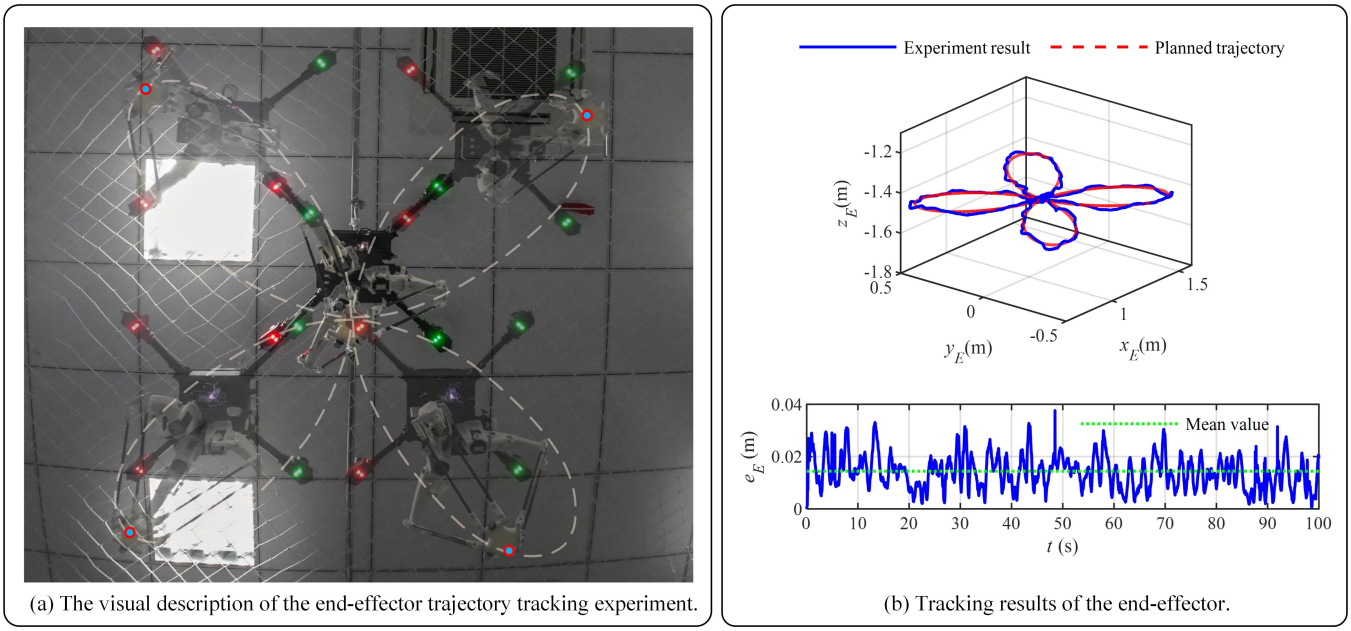

(a) The visual description of the end-effector trajectory tracking experiment.

(b) Tracking results of the end-effector.

Fig. 9: Results of the end-effector trajectory tracking experiment.

TABLE III: Measurement noises and inertia uncertainties of the Monte Carlo simulation.

Noises and uncertainties	Zero-mean Gaussian distribution	Uniform distribution
	Standard derivation	Range
Position noises	0.010 m	— —
Velocity noises	0.010 m/s	— —
Attitude angle noises	0.0175 rad	— —
Angular velocity noises	0.0175 rad/s	— —
Low inertia uncertainties	— —	±5%
Middle inertia uncertainties	— —	±10%
High inertia uncertainties	— —	±20%

TABLE IV: Mean values and standard derivations of the Monte Carlo simulation results.

Uncertainty level	Mean value of e_B (m)	Standard derivation of e_B (m)
Low	0.009	0.004
Middle	0.016	0.008
High	0.024	0.018

of uncertainty.

The mean values and the standard derivations of the position error of the quadcopter base in the Monte Carlo simulation results are shown in Table IV. With the proposed method, the mean values of the results in low, middle, and high uncertainties are 0.009 m, 0.016 m, and 0.024 m, respectively. The standard derivations of the results in the low, middle, and high uncertainties are 0.004 m, 0.008 m, and 0.018 m, respectively. The results demonstrate the robustness of the proposed method given different levels of uncertainties.

B. *Example 2: End-effector stabilization*

The control objective of this experiment is to stabilize the end-effector to a fixed position while the quadcopter is flying along a circle with a diameter of 0.12 m (see Fig. 8(a)). The size of the circle is limited by the size of the Delta arm's workspace to ensure the end-effector can reach the fixed position. The purpose of this experiment is to validate the P-P mode of the proposed cooperative planner together with the flight controller. This scenario considered in this experiment is important because practical tasks may require assigning separate trajectories for the quadcopter base and the end-effector. For example, the end-effector must track a desired trajectory to complete a manipulating task whereas the quadcopter base must move to avoid obstacles or observe the manipulating target from different angles using onboard cameras.

The control results are shown in Fig 8. First, it is shown in Fig 8(b) that the mean position error of the end-effector is 0.011 m. The standard deviation of the position error is 0.004 m. Second, the planned trajectories for the quadcopter base and Delta arm are shown in Fig 8(c). As can be seen, the mean tracking error of the quadcopter base can reach 0.018 m.

C. *Example 3: End-effector trajectory tracking*

The control objective in the third experiment is that the end-effector can accurately track a desired complex trajectory. The purpose of this experiment is to validate the E-P mode of the proposed cooperative planner together with the flight controller. Different from the second example, this example does not require specifying the desired trajectory of the quadcopter base.

The desired trajectory of the end-effector is set as a shape of a four-petal flower (Fig. 9(a)). In particular, let

This article has been accepted for publication in IEEE Transactions on Automation Science and Engineering. This is the author's version which has not been fully edited and content may change prior to final publication. Citation information: DOI 10.1109/TASE.2023.3260874

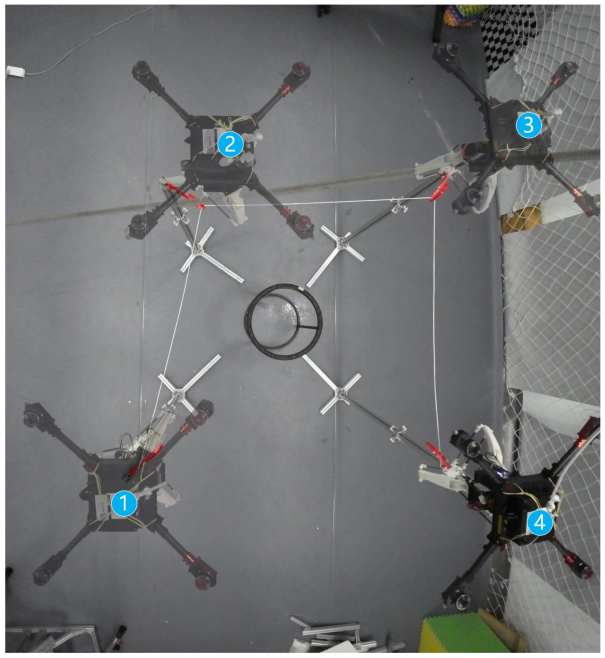

(a) Top view of the aerial weaving experiment.

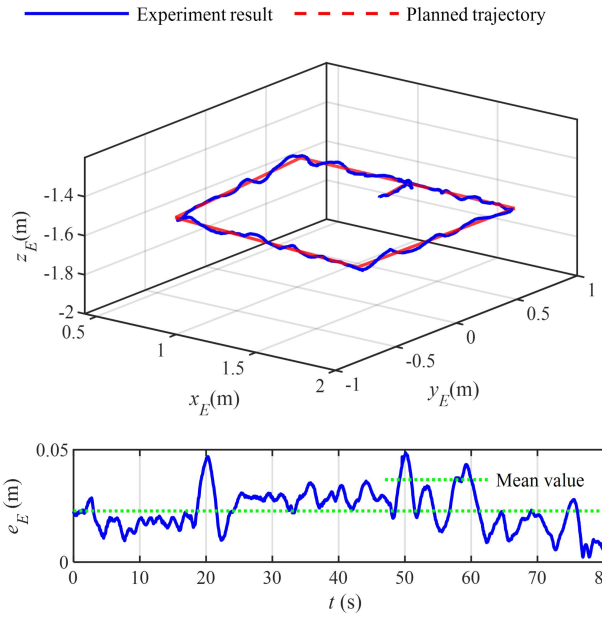

(c) Experiment results of the end-effector.

Fig. 10: Results of the aerial weaving experiment.

$\boldsymbol{p}_{E,0} = [x_{E,0}, y_{E,0}, z_{E,0}]^T$ be the initial position. The desired trajectory of the end-effector is designed as

$$\begin{aligned} x_{E,d} &= x_{E,0} + 0.3(1 - \cos 0.08\pi t) * \cos 0.02\pi t, \\ y_{E,d} &= y_{E,0} + 0.3(1 - \cos 0.08\pi t) * \sin 0.02\pi t, \\ z_{E,d} &= z_{E,0}. \end{aligned} \tag{73}$$

The tracking performance of the end-effector is shown in Fig. 9(b). The mean tracking error of the end-effector is as low as 0.01 m.

D. Example 4: Aerial weaving

In the final example, a rope is tied at the end-effector. The control objective is that the end-effector must pass through four hangers precisely and complete an aerial weaving task (see Fig. 1). The four hangers are mounted on the top of four pillars. A passive rope dispenser is mounted on one of the pillars. The rope must be pulled out from the dispenser by the aerial manipulator during the flight. Therefore, this example is more challenging than the third one because the aerial manipulator must overcome the drag force of the rope. Hence, this example can better demonstrate the robustness of the overall system in practical manipulation tasks.

The reference of the end-effector is calculated based on the positions of the hangers. The control is archived by the flight controller together with the E-P mode of the cooperative planner. As shown in Fig. 10, the task is completed by the proposed method. In particular, the mean tracking error of the end-effector is 0.02 m, which is greater compared to the third example where the mean tracking error is 0.01 m. This is reasonable due to the drag force of the rope. Since force control is not specifically considered in our algorithms, the present performance verifies the ability of the proposed algorithm to counter external forces applied to the end-effector.

VIII. Conclusion

This paper proposed an ESO-based approach for end-effector tracking control of an aerial manipulator. It is verified by four experimental results. The results of the disturbance rejection experiment show the mean position error of the quadcopter base with the proposed method is 0.02 m when the Delta arm swings fast with a payload of 1.2 kg. As a comparison, the mean position error of the quadcopter base with the PX4 controller is 0.09 m. The mean tracking errors of the end-effector stabilization and the end-effector trajectory tracking experiments are 0.011 m and 0.01 m, respectively. In the aerial weaving experiment, the mean tracking error of the end-effector is 0.02 m. These results verify that the proposed approach can achieve accurate and robust control performance. The approach requires minimal measurement information and hence can be implemented conveniently in real time. Although force control is not specifically addressed in this approach, the ESOs can estimate external disturbances applied to the end-effector to a certain extent. It is verified by the aerial weaving experiment that the aerial manipulator with the proposed method can accomplish the experiment under the drag force of the rope. The entire system shows certain robustness against external forces. However, in order to handle strong force interaction between the manipulator and the environment, force sensors and force control must be introduced. This will be one important research direction for future research.

REFERENCES

[1] N. Staub, D. Bicego, Q. Sablé, V. Arellano, S. Mishra, and A. Franchi, "Towards a flying assistant paradigm: the othex," in *2018 IEEE International Conference on Robotics and Automation (ICRA)*, pp. 6997–7002, IEEE, 2018.

[2] K. Steich, M. Kamel, P. Beardsley, M. K. Obrist, R. Siegwart, and T. Lachat, "Tree cavity inspection using aerial robots," in *2016 IEEE/RSJ International Conference on Intelligent Robots and Systems (IROS)*, pp. 4856–4862, IEEE, 2016.

[3] M. Tognon, H. A. T. Chávez, E. Gasparin, Q. Sablé, D. Bicego, A. Mallet, M. Lany, G. Santi, B. Revaz, J. Cortés, *et al.*, "A truly-redundant aerial manipulator system with application to push-and-slide inspection in industrial plants," *IEEE Robotics and Automation Letters*, vol. 4, no. 2, pp. 1846–1851, 2019.

[4] M. Orsag, C. Korpela, S. Bogdan, and P. Oh, "Valve turning using a dual-arm aerial manipulator," in *2014 International Conference on Unmanned Aircraft Systems (ICUAS)*, pp. 836–841, IEEE, 2014.

[5] W. Dong, Z. Ma, X. Sheng, and X. Zhu, "Centimeter-level aerial assembly achieved with manipulating condition inference and compliance," *IEEE/ASME Transactions on Mechatronics*, 2021.

[6] A. Ollero, M. Tognon, A. Suarez, D. Lee, and A. Franchi, "Past, Present, and Future of Aerial Robotic Manipulators," *IEEE Transactions on Robotics*, 2021.

[7] D. Xilun, G. Pin, X. Kun, and Y. Yushu, "A review of aerial manipulation of small-scale rotorcraft unmanned robotic systems," *Chinese Journal of Aeronautics*, vol. 32, no. 1, pp. 200–214, 2019.

[8] V. Lippiello and F. Ruggiero, "Cartesian impedance control of a UAV with a robotic arm," *IFAC Proceedings Volumes*, vol. 45, no. 22, pp. 704–709, 2012.

[9] A. Suarez, A. Jimenez-Cano, V. Vega, G. Heredia, A. Rodriguez-Castaño, and A. Ollero, "Lightweight and human-size dual arm aerial manipulator," in *2017 International Conference on Unmanned Aircraft Systems (ICUAS)*, pp. 1778–1784, IEEE, 2017.

[10] J. Thomas, G. Loianno, J. Polin, K. Sreenath, and V. Kumar, "Toward autonomous avian-inspired grasping for micro aerial vehicles," *Bioinspiration & Biomimetics*, vol. 9, no. 2, p. 025010, 2014.

[11] F. Ruggiero, M. A. Trujillo, R. Cano, H. Ascorbe, A. Viguria, C. Peréz, V. Lippiello, A. Ollero, and B. Siciliano, "A multilayer control for multirotor UAVs equipped with a servo robot arm," in *2015 IEEE international conference on robotics and automation (ICRA)*, pp. 4014–4020, IEEE, 2015.

[12] A. Jimenez-Cano, J. Braga, G. Heredia, and A. Ollero, "Aerial manipulator for structure inspection by contact from the underside," in *2015 IEEE/RSJ international conference on intelligent robots and systems (IROS)*, pp. 1879–1884, IEEE, 2015.

[13] G. Zhang, Y. He, B. Dai, F. Gu, J. Han, and G. Liu, "Robust control of an aerial manipulator based on a variable inertia parameters model," *IEEE Transactions on Industrial Electronics*, vol. 67, no. 11, pp. 9515–9525, 2019.

[14] K. Bodie, M. Tognon, and R. Siegwart, "Dynamic end effector tracking with an omnidirectional parallel aerial manipulator," *IEEE Robotics and Automation Letters*, vol. 6, no. 4, pp. 8165–8172, 2021.

[15] Y. Chen, W. Zhan, B. He, L. Lin, Z. Miao, X. Yuan, and Y. Wang, "Robust control for unmanned aerial manipulator under disturbances," *IEEE Access*, vol. 8, pp. 129869–129877, 2020.

[16] A. E. Jimenez-Cano, J. Martin, G. Heredia, A. Ollero, and R. Cano, "Control of an aerial robot with multi-link arm for assembly tasks," in *2013 IEEE International Conference on Robotics and Automation*, pp. 4916–4921, IEEE, 2013.

[17] H. Yang and D. Lee, "Dynamics and control of quadrotor with robotic manipulator," in *2014 IEEE International Conference on Robotics and Automation (ICRA)*, pp. 5544–5549, IEEE, 2014.

[18] K. Baizid, G. Giglio, F. Pierri, M. A. Trujillo, G. Antonelli, F. Caccavale, A. Viguria, S. Chiaverini, and A. Ollero, "Behavioral control of unmanned aerial vehicle manipulator systems," *Autonomous Robots*, vol. 41, no. 5, pp. 1203–1220, 2017.

[19] G. Muscio, F. Pierri, M. A. Trujillo, E. Cataldi, G. Antonelli, F. Caccavale, A. Viguria, S. Chiaverini, and A. Ollero, "Coordinated control of aerial robotic manipulators: theory and experiments," *IEEE Transactions on Control Systems Technology*, vol. 26, no. 4, pp. 1406–1413, 2017.

[20] E. Cataldi, F. Real, A. Suárez, P. Di Lillo, F. Pierri, G. Antonelli, F. Caccavale, G. Heredia, and A. Ollero, "Set-based inverse kinematics control of an anthropomorphic dual arm aerial manipulator," in *2019 International Conference on Robotics and Automation (ICRA)*, pp. 2960–2966, IEEE, 2019.

[21] D. Lunni, A. Santamaria-Navarro, R. Rossi, P. Rocco, L. Bascetta, and J. Andrade-Cetto, "Nonlinear model predictive control for aerial manipulation," in *2017 International Conference on Unmanned Aircraft Systems (ICUAS)*, pp. 87–93, IEEE, 2017.

[22] G. Heredia, A. Jimenez-Cano, I. Sanchez, D. Llorente, V. Vega, J. Braga, J. Acosta, and A. Ollero, "Control of a multirotor outdoor aerial manipulator," in *2014 IEEE/RSJ International Conference on Intelligent Robots and Systems*, pp. 3417–3422, IEEE, 2014.

[23] P. Chermprayong, K. Zhang, F. Xiao, and M. Kovac, "An integrated delta manipulator for aerial repair: A new aerial robotic system," *IEEE Robotics & Automation Magazine*, vol. 26, no. 1, pp. 54–66, 2019.

[24] M. Muller, "A novel classification of planar four-bar linkages and its application to the mechanical analysis of animal systems," *Philosophical Transactions of the Royal Society of London. Series B: Biological Sciences*, vol. 351, no. 1340, pp. 689–720, 1996.

[25] B. Siciliano, L. Sciavicco, L. Villani, and G. Oriolo, *Robotics: modelling, planning and control*. Springer Science & Business Media, 2010.

[26] M. López, E. Castillo, G. García, and A. Bashir, "Delta robot: inverse, direct, and intermediate Jacobians," *Proceedings of the Institution of Mechanical Engineers, Part C: Journal of Mechanical Engineering Science*, vol. 220, no. 1, pp. 103–109, 2006.

[27] X. Yang, Z. Feng, C. Liu, and X. Ren, "A geometric method for kinematics of Delta robot and its path tracking control," in *2014 14th International Conference on Control, Automation and Systems (ICCAS 2014)*, pp. 509–514, IEEE, 2014.

[28] J. E. Shigley, C. R. Mischke, and T. H. Brown Jr, *Standard handbook of machine design*. McGraw-Hill Education, 2004.

[29] Q. Zheng, L. Q. Gaol, and Z. Gao, "On stability analysis of active disturbance rejection control for nonlinear time-varying plants with unknown dynamics," in *2007 46th IEEE conference on decision and control*, pp. 3501–3506, IEEE, 2007.

[30] R. Fabre, Q. Rouxel, G. Passault, S. NGuyen, and O. Ly, "Dynaban, an open-source alternative firmware for dynamixel servo-motors," in *Robot World Cup*, pp. 169–177, Springer, 2016.

[31] H. K. Khalil, *Nonlinear systems*, vol. 3. Prentice hall Upper Saddle River, NJ, 2002.

[32] T. Lee, "Robust adaptive attitude tracking on SO(3) with an application to a quadrotor UAV," *IEEE Transactions on Control Systems Technology*, vol. 21, no. 5, pp. 1924–1930, 2012.

[33] S. Bandyopadhyay, S.-J. Chung, and F. Y. Hadaegh, "Nonlinear attitude control of spacecraft with a large captured object," *Journal of Guidance, Control, and Dynamics*, vol. 39, no. 4, pp. 754–769, 2016.

[34] A. Del Prete, "Joint position and velocity bounds in discrete-time acceleration/torque control of robot manipulators," *IEEE Robotics and Automation Letters*, vol. 3, no. 1, pp. 281–288, 2017.

[35] P. Ramon Soria, B. Arrue, and A. Ollero, "A 3D-printable docking system for aerial robots: Controlling aerial robotic manipulators in outdoor industrial applications," *IEEE Robotics Automation Magazine*, vol. 26, no. 1, pp. 44–53, 2019.

[36] R. Verdn, G. Ramrez, C. Rivera, and G. Flores, "Teleoperated aerial manipulator and its avatar. communication, system's interconnection, and virtual world," in *2021 International Conference on Unmanned Aircraft Systems (ICUAS)*, pp. 1488–1493, 2021.

[37] Y. Sun, Z. Jing, P. Dong, J. Huang, W. Chen, and H. Leung, "A switchable unmanned aerial manipulator system for window-cleaning robot installation," *IEEE Robotics and Automation Letters*, vol. 6, no. 2, pp. 3483–3490, 2021.

Huazi Cao received the B.Eng. degree from the Harbin Engineering University, Harbin, China, in 2013, and the Ph.D. degree from the Beihang University, Beijing, China, in 2018. From 2018 to 2019, he was a Research Scientist with the Southwest China Research Institute of Electronic Equipment, Chengdu, China. He is currently a Research Fellow at the Intelligent Unmanned Systems Laboratory in the School of Engineering, Westlake University, Hangzhou, China. His research interests include control and planning of aerial robots.

This article has been accepted for publication in IEEE Transactions on Automation Science and Engineering. This is the author's version which has not been fully edited and content may change prior to final publication. Citation information: DOI 10.1109/TASE.2023.3260874

Yongqi Li received the B.Eng. degree in electrical engineering from the Hunan University of Arts and Science, Changde, China, in 2020. He was a corecipient of the Second Prize of the National Undergraduate Electronics Design Contest, Shanghai, China, in 2019, and the Second Prize of the lnteligent Robot Fighting Competition, Hangzhou, China, in 2019. He is currently an Embedded System Engineer at the Intelligent Unmanned Systems Laboratory in the School of Engineering, Westlake University, Hangzhou, China. His research focuses on hardware and software development of aerial robots.

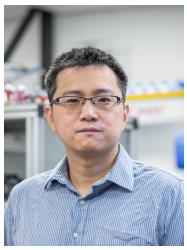

Cunjia Liu received a Ph.D. in autonomous vehicle control from Loughborough University in 2011, where he became an academic in 2013 and was promoted to a Reader in Unmanned Vehicles in 2021.

He has a strong background in flight control, autonomous vehicles, and Bayesian estimation. His recent work focuses on the novel information gathering and planning algorithms for autonomous robotics and their applications in defence, security, environment monitoring and precision agriculture. He currently serves as the Associate Editor for IEEE Robotics and Automation Letters and IEEE Robotics & Automation Magazine.

Shiyu Zhao (Member, IEEE) received the B.Eng. and M.Eng. degrees from the Beijing University of Aeronautics and Astronautics, Beijing, China, in 2006 and 2009, respectively, and the Ph.D. degree from the National University of Singapore, Singapore, in 2014, all in electrical engineering.

From 2014 to 2016, he was a Postdoctoral Researcher with the Technion-Israel Institute of Technology, Haifa, Israel, and the University of California at Riverside, Riverside, CA, USA. From 2016 to 2018, he was a Lecturer with the Department of Automatic Control and Systems Engineering, University of Sheffield, Sheffield, U.K. He is currently an Associate Professor with the School of Engineering, Westlake University, Hangzhou, China. His research focuses on theories and applications of robotic systems.